# Droplet Migration through Deformable Stenosed Microchannel: Dynamics and Blockage

Kumar Amit (कुमार अमित)[a], Ashwani Assam (अश्वनी असम)[a], and Abhishek Raj (अभिषेक राज)[a,b]

[a]Department of Mechanical Engineering, IIT Patna, Bihar-801106, India

[b] Corresponding author: araj@iitp.ac.in

## ABSTRACT

Understanding droplet migration in stenosed microchannels is crucial for various applications. This study explores how droplet properties (viscosity, surface tension, density, and diameter) and channel characteristics (stenosis degree and wall elasticity) affect droplet movement and blockage in deformable stenosed microchannels. Higher viscosities lead to lubrication film formation between droplet and wall, reducing viscous resistance; while increased surface tension enhances wall adherence, amplifying Laplace pressure. Droplet entry is primarily influenced by viscosity, while passage is governed by surface tension and curvature effects at the droplet-wall interface. Surface tension dominates pressure generation in the channel and within the droplet, influencing wall deformation and hydrodynamic resistance. The study examines the relationship between droplet viscosity, density, surface tension, channel wall elasticity, and the maximum Capillary number ($Ca_{max}$) on the lubrication film thickness between the droplet and the channel wall. A lubrication film exists for $Ca_{max} \geq 0.095$, reducing blockage chances. A critical range of the modified Ohnesorge Number ($Oh^* \times 1000 \leq 132$) and Capillary number ($Ca_{max} < 0.095$) indicates higher chances of droplet blockage. The blockage prediction method based on the modified Ohnesorge exhibits a sensitivity of 100%, specificity of 92.6%, and accuracy of 95.9%. Additionally, the study explores the impact of channel wall elasticity on droplet entry, transit, and hydrodynamic resistance. Higher wall elasticity facilitates faster entry but introduces curvature during passage, increasing frictional resistance and blockage likelihood as the wall softens.

**Keywords**: Atherosclerosis, Stenosed microchannel, Deformable, Fluid-structure interaction (FSI), Volume of fluid (VOF), Lubrication film thickness (*LFT*), Ohnesorge number, Capillary Number, Stenosed deformable blood vessel

## I. INTRODUCTION

Droplets play a vital role in the successful design and development of numerous microfluidic Lab on Chip devices involving various chemical and biological processes [1–4]. Droplet migration through confined microchannel is often utilized in diverse applications, such as biological reactions [5], fuel cells [6], Micro-electro-mechanical-systems (MEMS) [7], flow through porous media [8], and bio-printing [9–11]. Droplets are often also used to mimic biological cells [10–16]. Thus, droplet migration through confined microchannel can provide valuable insights about cell migration through stenosed blood vessels [11,13]. Hence, the fundamental understanding of droplet migration through narrow confinements is crucial.

There have been few fundamental investigations on droplet migrations through confined microchannels [2,15,17–23]. Zhang et al. [17] investigated the passage behavior of highly viscous droplets through confined microchannels. They report that the droplet viscosity influences the flow velocity and the pressure drop across the confined channel. However, the effect of the droplet's surface tension, density, and diameter on the passage behavior was not investigated in their work. Zhang et al. [19] contributed a comprehensive review of narrow confinements, emphasizing key parameters and identifying open research challenges. Zhang et al. [24] investigated the impulse or momentum change associated with squeezing a droplet through a narrow circular constriction. The authors developed an analytical expression for the minimum impulse and the corresponding critical velocity. The study provides insights on droplet squeezing and impact dynamics, offering valuable insights into the influence of surface tension, viscosity, and channel geometry on the transport process. Leong et al. [14] numerically investigates the deformation and entry of droplets into a constricted microchannel, with implications for applications in cell sorting

and cancer diagnostics. The study explores the influence of droplet mechanical properties on entry time and deformation profiles, while acknowledging limitations such as neglecting droplet-wall contact and wall deformability. Singla et al. [2] reviewed the impact of surface topography on droplet and bubble flow through constricted passages, highlighting the importance of parameters like Capillary number, viscosity, and diameter ratios. Recently, Wang et al. [20] conducted a numerical investigation into the deformation of droplets in microchannels, emphasizing its potential applications in cell sorting devices based on mechanical properties. Most of these studies have not delved upon the entry process in terms of dependency on different fluid and wall properties and the influence of droplet motion on wall-shear stress ($WSS$) at the constriction walls.

All previously cited literature has examined the motion of drops within confined microchannels featuring rigid walls. Some studies have employed two-dimensional analyses [14,17,24–28], while others have utilized three-dimensional models, both numerical and experimental, with rectangular or square cross-sectional rigid micro-confinements [15,16,20,29–31]. Nonetheless, research on droplet migration through microchannels with flexible walls is very limited. In this regard, Raj et al. [32] explored the impact of wall compliance on droplet mobility through deformable, non-confined microchannels, underlining the significance of wall deformability. Subsequently, Raj and Sen [33] underscored the crucial influence of wall compliance on the migration behavior of deformable objects through constricted microchannels, utilizing a combination of experimental and theoretical approaches. In summary, the effects of droplet properties such as viscosity, density, and surface tension on migration behavior through a deformable stenosed region remain largely unexplored. To address this gap, the current study offers a comprehensive investigation into the influence of droplet properties and wall elasticity on migration dynamics within a deformable, confined, and three-dimensional microchannel.

The lubrication film, a thin fluid layer separating droplets from microchannel walls, is integral to droplet dynamics, especially in narrow channels [34]. Its thickness depends on the balance between capillary and viscous forces influencing droplet motion [17,34]. This film affects the droplet's shape and speed by introducing significant intermolecular forces. Studies, such as by Zhang et al. [17], qualitatively report an increase in lubrication layer thickness with viscosity ratio. Khan et al. [15] paralleled these findings, investigating viscous droplets migrating in microchannels, particularly in terms of friction forces and lubrication film thickness. Recently, Tang et al. [21] have introduced a quick method for estimating transit time for droplets passing through the constriction channel, considering the lubrication film and exploring its dependency on parameters like pressure, viscosity, pore dimensions, and surface tension. However, quantitative estimations of the effect of droplet properties on the lubricating film thickness are not very well understood, which is reported in the current work. The present study uniquely delves into quantifying lubrication film thickness ($LFT$), and examining its correlation with viscosity ratio, surface tension ratio, Capillary number, and Ohnesorge number, which is a novel contribution to the field. Notably, the present study extends the investigation to consider the potential impact of wall stiffness on $LFT$, a factor that, to the best of authors knowledge, has not been explored till date.

Anticipating and preventing blockages in microfluidic systems is pivotal for ensuring the seamless and uninterrupted flow of droplets within channels. This aspect, which has been somewhat overlooked, is the main focus of the present study. This is essential for the efficiency and accuracy of applications spanning medical diagnostics, especially for diseases arising due to blood vessel blockage, such as cardiovascular diseases like strokes and heart attacks, chemical analysis, and drug delivery. Accurate blockage prediction not only enhances the overall stability and performance of microfluidic devices but also informs optimized design and operational strategies in diseases arising due to flow blockage. By addressing potential disruptions, this predictive capability contributes significantly to the reliability and success of microfluidic technologies, playing a crucial role in advancing scientific research and technological innovations.

As mentioned above, the droplet through a confined microchannel holds much importance in microfluidics. It can be noted that the narrow passage or the confinement often gets blocked, for example, Atherosclerosis leading to

stenosed condition, i.e., narrowed blood vessel, is a common phenomenon that occurs in arteries due to the accumulation of plaque on the arterial walls. This can lead to reduced blood flow (blockages) and an increased risk of fatal diseases due to insufficient blood supply, such as ischemic strokes and heart attacks [35,36]. There have been recent findings that wall shear stress ($WSS$) can contribute to the development of high-risk plaques [37,38]. A high $WSS$ can cause changes in the behaviour of endothelial cells, leading to increased inflammation and growth of the atherosclerotic lipid core. Therefore, the prediction of such stroke like conditions, i.e., the blockages of blood vessels, would involve understanding their cause in terms of local factors such as wall shear stress, flow velocity, pressure distribution, geometry, and the degree of stenosis. Investigation into the effect of droplet properties (such as viscosity, surface tension, density, and diameter) on the migration process, $WSS$ and the hydrodynamic resistance; and the corresponding chance of stroke also carries significant importance. A preliminary study utilizing liquid droplet motion through a stenosed deformable microchannel thus has the potential to throw more insights into such dynamics and blockages.

In the current work, we present the possibility of predicting the blockage of liquid droplets migrating through a deformable stenosed microchannel using modified critical "*Ohnesorge Number* ($Oh^*$)" and "*Capillary number* ($Ca_{max}$)". The insights from this study can enhance the prediction of cardiovascular diseases caused by blood vessel blockages, using a more complex cell model. Our objective, here, is to explore the relationship between various physical properties influencing droplet motion through a three-dimensional deformable stenosed microchannel, which can lead to blockages. We examine the entry and transit processes within such a microchannel to identify the range of the Ohnesorge number, which can serve as an indicator for potential complete blockage scenarios.

The main novelty and significance of the current work are as follows:

1. To the best of the authors' knowledge, this is the first work presenting a detailed numerical investigation of the migration of liquid droplets with finite surface tension value through a novel deformable stenosed microchannel. The model can be very useful in mimicking cell migration through the deformable stenosed blood vessel.

2. The investigation of the entry and passage process in the current work is more comprehensive incorporating the following aspects: (a) pressure in the channel and inside the droplet, (b) Capillary number, (c) $WSS$, (d) droplet velocity, (e) contact line (f) entry and passage time, (g) inertial effect, (h) channel wall curvature effect, (i) channel wall stiffness and deformation, and (j) hydrodynamic resistance, (k) Effect of viscosity, density, surface tension and diameter.

3. A modified *Ohnesorge Number* ($Oh^*$) is proposed. A critical range of modified *Ohnesorge Number* ($Oh^*$) and "*Capillary number* ($Ca_{max}$) is identified, in which the chances of droplet blockage are maximum.

4. Effect of droplet's viscosity, density, surface tension, and diameter; degree of stenosis; and $Oh^*$ on the entry and transit time is presented.

5. The effect of channel wall elasticity on the droplet entry, transit, $LFT$ and hydrodynamics resistance is presented.

6. The effect of droplet viscosity, density, surface tension, channel wall elasticity, $Oh^*$ and $Ca$ on the lubrication film thickness between the droplet and the channel wall is presented.

The outline of the current work is as follows. First, the problem is described in detail, along with the material properties used in the analysis in Sec. II. Thereafter, numerical technique is described in Sec. III. Next, different

parameters are introduced in Sec. IV. In Sec. V, experimental setup and model validation are presented, which follow the results and discussion in Sec. VI. The effect of viscosity, surface tension, density, diameter, and stiffness on the entry process is investigated in Sec. VI A. In Sec. VI B, the droplet-passage process is analyzed for the passing time and the pressure developed across the stenosed region. The hydrodynamic resistance developed across a stenosed channel is compared with the non-stenosed channel in Sec. VI C. Subsequently, a modified Ohnesorge number is developed and presented in Sec. VI D, which has been used as a tool for predicting the scenario of complete blockage in a stenosed microchannel. Also, VI E presents the investigation on the effect of wall elasticity on the droplet migration process. Finally, Sec. VII summarizes the key findings and novelties of the present work.

## II. PROBLEM DESCRIPTION

The schematic in Fig. 1 (a) shows the isometric view of the three-dimensional model used in this study. The Fig. 1 (b) shows the droplet in the stenosed region. At this instant, a zoomed view of the top-wall vicinity is shown in Fig. 1 (c), where the calculation of the wall deformation and the lubrication film is illustrated (Multimedia view). In the simplified but helpful hydraulic model, it is possible to illustrate the relationship between the flow through a deformable stenosed microchannel, collateral flow, and frictional resistance. The computational domain consists of both the solid and fluid domains, with the latter comprising dispersed and continuous phases that are assumed to be incompressible. Figures 1 (d) and (e), respectively, depict the pressure drop across the stenosed region and the wall deformation variation with respect to time. The parametric detail of the computational domain is shown in Fig. 1 (a). In the solid domain, the bottom wall has a plaque-like structure ($t = 37\ \mu m$), creating stenosis in the microchannel, and the top wall has a thin deformable portion ($h = 10\ \mu m$) mimicking the non-stenosed deformable portion of the stenosed microchannel. It should be noted that the bottom stenosed wall is modeled as a non-rigid structure, but due to its larger thickness, it undergoes negligible deformation. It is noteworthy that the migration of the droplet through a confined microchannel closely resembles the motion of cells through a stenosed blood vessel. The liquid-droplet model for modeling a biological cell assumes that the cell is composed of a homogenous liquid encapsulated by a cortical membrane. The cortical membrane is characterized as an anisotropic viscous fluid layer with a constant surface tension [39]. Many previous studies have discussed liquid droplet-like characteristics of cells and used the same in their modeling approaches [12–14]. The liquid droplet model serves as a valuable tool in elucidating the complex dynamics of cells within blood vessels, offering a computational framework to better understand physiological and pathological processes. Various sophisticated models have been developed to mimic cell migration through blood vessels [14,25,40–44], but the simplicity and computational efficiency of a liquid droplet model make it a compelling choice. This simpler model retains the ability to capture essential cell-like physics, requiring minimal computational resources and facilitating ease in modeling [11,24,26]. The significance of choosing the liquid droplet model becomes evident in its widespread applications, ranging from analyzing motion dynamics to predicting blockages in narrow blood vessels.

In the present study, a spherical liquid droplet is infused through the stenosed section with a constant velocity (= $0.5\ m/s$) (Fig. 1 a) and through the channel inlet, the continuous phase liquid enters at a constant flow rate ($Q$) of $7.92\ \mu l/min$. The outlet is assumed to be at atmospheric pressure. The material properties (density $\rho_c = 1000\ kg/m^3$, viscosity $\mu_c = 0.005\ kg/m$-s) of the continuous phase, which resembles blood plasma [45,46] through a stenotic vessel, is kept the same for all simulations. The viscosity of plasma in a normal blood vessel is ~0.001 $kg/m$-s. However, it has been observed that the plasma viscosity is higher in a stenotic blood vessel than in a healthy vessel [45,46] and therefore $\mu_c = 0.005\ kg/m$-s has been used in this study. The material properties for the fluid and solid domains are tabulated in Table 1. The deformable stenosed portion and the deformable wall above the stenosed portion is modeled using Polydimethylsiloxane (PDMS) material, as is commonly done in literature [47], whose properties are taken from different literature [48,49]. The wall is assumed to be non-wetting in this study to ignore the sticking nature of the stenosed region [50].

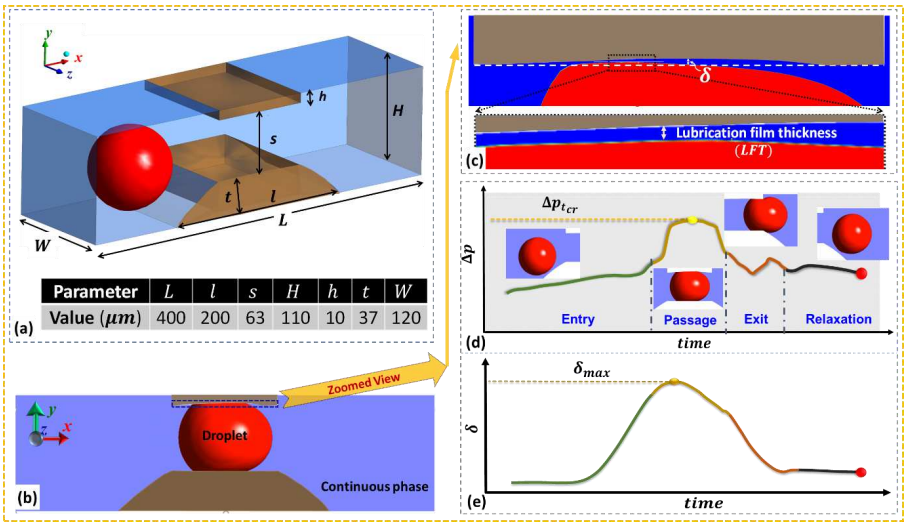


**Fig. 1.** Schematic of (a) the isometric view of the simulated 3D model with the parametric definition at the time when the flow is about to onset, and (b) the side-view (x-y plane) of the model used in the study. The deformable solid domain is shown with a brown colour. (c) The zoomed view near the top wall showing the wall deformation and the lubrication film thickness. The schematic of (d) the pressure across the stenosed region, and (e) the wall deformation with time. (Figures a-c: produced using 3D FSI simulation) (Multimedia view)

Table 1: Material properties for fluid and solid domains.

| Domain | Material | Density (kg/m$^3$) | Viscosity (N-s/m$^2$) | Surface tension (N/m) |
|---|---|---|---|---|
| Fluid | Continuous phase | 1000 | 0.005 | 0.0005-0.02 |
| | Dispersed phase | 400-1500 | 0.0005-0.02 | |

| Domain | Material | Density (kg/m$^3$) | Young's Modulus (MPa) | Poisson's ratio |
|---|---|---|---|---|
| Solid | Polydimethylsiloxane | 965 | 0.1-1 | 0.499 |

## III. NUMERICAL METHOD

Combining fluid-structure interaction (FSI) and volume of fluid (VOF) methods for simulation can provide a powerful tool for simulating and performing a comprehensive study of complex fluid-structure systems, such as those found in the flow behaviour of blood vessels. One of the main challenges associated with conducting coupled FSI simulations is the need for higher computational cost due to the requirement of solving two independent physics fields - fluid dynamics and structural mechanics - simultaneously at each time step, as well as exchanging data between the two fields. In the present study, we opted for a small section of the stenosed microchannel for the

simulation. The aim is to analyse the flow behaviour in the channel's stenosed region and investigate the effect of the wall deformability and stenosed region inside the channel with minimal use of computational resources. The two-way FSI approach in ANSYS Workbench [51] couples fluid and solid domains. The fluid domain has two-liquid phases. The interface between the two phases is tracked using the unsteady volume of fluid (VOF) method [52]. The solid domain is solved using the transient structural component of ANSYS Mechanical [51].

### A. Governing Equations

#### 1. *Fluid domain*

A single set of momentum equations is solved in the VOF approach, which then tracks the volume fraction of each fluid throughout the domain to describe two or more immiscible fluids [53]. Here, the liquid used for the spherical droplet is chosen to be the primary phase, while liquid flowing throughout the channel is prescribed as the secondary phase. In the VOF method, the volume fraction equation (Eq. 1) and the momentum equation (Eq. 4) are solved. The flow is considered to be incompressible, and the gravity effect is neglected. The volume fraction equation [53] is given as:

$$\frac{\partial \varphi}{\partial t} + \nabla \cdot (\varphi \vec{v}) = 0 \tag{1}$$

where, $\varphi$ and $\vec{v}$ are the volume fraction and the averaged velocity vector, respectively. Here, $\varphi = 1$ denotes cells in the computational domain are filled with the secondary phase and $\varphi = 0$ denotes the presence of the primary phase only. The value of $0 \leq \varphi \leq 1$ represents the interface between the two phases. The compliant walls will deform due to the flowing fluid, which in turn will impose force on the fluid and alter the flow through the channel. A two-way coupling approach is more effective in such circumstances [54]. The same procedure is adopted in the present study by using "System-Coupling" module in Ansys 19.1 Workbench [51].

The phase average density ($\rho$) and viscosity ($\mu$) in a computational cell can be given in terms of $\varphi$ as [53]

$$\text{Mixture density, } \rho = \rho_2 \varphi + (1 - \varphi)\rho_1 \tag{2}$$

$$\text{Mixture viscosity, } \mu = \mu_2 \varphi + (1 - \varphi)\mu_1 \tag{3}$$

where subscripts 1 and 2 denote primary and secondary, respectively.

Besides keeping track of the interface, the simulation also needs to consider the impact of surface tension. The surface tension model is based on the continuum surface force (CSF) method. When adding surface tension to the VOF calculation, it appears as a source term in the regular incompressible Navier-Stokes equation. The momentum equation for the entire computational domain is solved, which enables the distribution of the velocity field between the two phases [53,55],

$$\rho \frac{\partial \vec{v}}{\partial t} + \rho \nabla \cdot (\vec{v}\vec{v}) = -\nabla p + \mu \nabla \cdot (\nabla \vec{v}) + \overrightarrow{S_t} \tag{4}$$

Here, $p$ and $S_t$ are the static pressure and the surface tension force, respectively. Eq. 4 is dependent on the volume fractions of both phases through the fluid properties, $\rho$ and $\mu$.

The force arising from surface tension can be converted into a volume force in the proximity of the interface and can be mathematically represented as [55]

$$\overrightarrow{S_t} = \sigma \frac{2\rho k \nabla \varphi}{(\rho_1 + \rho_2)} \tag{5}$$

Where $\sigma$ represents the interfacial tension coefficient between the two phases, while $k$ denotes the mean curvature of the interface within the control volume.

*2. Solid domain*

The transient structural solver uses Eq. 6 [56] to solve the basic equation for the displacement of linear, isotropic PDMS material [54,57,58], i.e., for the solid domain depicted in Fig. 1.

$$[S]\{x\} = \{V(t)\} \tag{6}$$

where, $[S]$ is the stiffness matrix, $\{x\}$ is the displacement vector and $\{V(t)\}$ is the acting load vector. In order to couple the fluid and solid equations, the system coupling approach is adopted. In their respective domains, the fluid and structural domains are explicitly solved. The coupling code functions as a "black box" and creates a data transfer mechanism for data exchange between the two solvers. The physics of the fluid and structural field are addressed individually and then connected by exchanging information through the fluid-solid interfaces. The simulation methodology is similar to our previous work [59], where we also solved transient two-way FSI by combining multiphase and structural deformation.

To compute pressure-velocity coupling, the "coupled with volume fractions" algorithm is employed. For gradient spatial discretization, "least squares cell-based" scheme is used. Similarly, the PRESTO method is utilized for pressure discretization, and the second-order upwind scheme is used for the momentum equation, while volume fraction equation is discretized through compressive scheme. The governing equations temporal components are discretized using a second-order implicit differencing scheme.

## IV. PARAMETER DEFINITIONS

The dimensionless numbers used in this study to simplify calculations, highlight important physical effects and facilitate ease in comparing different physical systems are presented in this section. The material and geometrical properties of the droplet have been normalised as follows:

$$\text{Normalised droplet viscosity, } \mu^* = \frac{\mu_d}{\mu_c} \tag{7}$$

where, $\mu_d$ and $\mu_c$ are the dynamic viscosities of the dispersed (droplet) and the continuous phases [2], respectively. In the study, the normalized droplet viscosity ranges from 0.1 to 4. In the study, we are also considering the effect of the viscosity-induced pressure. This is different from the study of Zhang et al. [24], where the viscosity ratio was 1, and thus disregarded the effect of the viscosity-induced pressure.

$$\text{Normalized droplet density, } \rho^* = \frac{\rho_d}{\rho_c} \tag{8}$$

where, $\rho_d$ and $\rho_c$ are respectively the densities of the dispersed and continuous phases. It ranges between 0.4 and 1.5.

The interfacial tension or the surface tension of the droplet is non-dimensionalised by using the cortical tension value of WBCs [60]. The normalized surface tension value for the droplet is given as, $\sigma^* = \sigma/\sigma_w$, where $\sigma$ and $\sigma_w$ are the surface tension of droplet and the cortical tension of WBCs, respectively. Here, $\sigma_w$ is taken as $4 \times 10^{-4}$ $N/m$, from the literature [60]. Notably, non-dimensionalizing the droplet's interfacial tension using WBC's cortical tension can be useful. This allows insights from our work to aid in understanding the migration of white blood cells or, cell clumps through stenosed, deformable blood vessels, where cortical tension influences the process. The ratio of droplet interfacial tension to WBC cortical tension provides a relative measure of their magnitudes. Examining

the effect of non-dimensionalized interfacial tension $\sigma^*$ on migration behavior illuminates how WBC stiffness influences its movement. Thus, integrating WBC cortical tension enhances understanding and can aid application to cardiovascular diseases like atherosclerosis. Note that alternative parameters for non-dimensionalization can be chosen based on specific applications.

The normalised droplet diameter is given by $D^*$, expressed as

$$\text{Normalised droplet diameter, } D^* = \frac{D}{s} \tag{9}$$

where, $D$ and $s$ are respectively the droplet diameter and the stenosed gap. This parameter discusses about the relative size of the droplet with respect to the gap in the stenosed portion of the channel.

The normalised wall stiffness is given by $Y^*$, expressed as

$$\text{Normalised wall stiffness, } Y^* = \frac{Y}{Y_a} \tag{10}$$

where, $Y$ and $Y_a$ are the stiffness of the wall and the artery. Here, the arterial stiffness is taken from the literature, as $Y_a = 0.5\ MPa$ [61].

Other dimensionless numbers that are used to analyse and describe the behaviour of the multiphase flows are described below [22]:

$$\text{Capillary number, } Ca_{max} = \frac{\mu_d u_{in}}{\sigma} \tag{11}$$

$u_{in}$ is the maximum speed that droplet attains while moving across the stenosed region of the channel.

Other than the aforementioned non-dimensional numbers, Ohnesorge number and its modified proposed form has been explained in Sec. VI D.

The degree of stenosis can be defined as

$$\text{Degree of stenosis} = (\{1 - s/(H - h)\} * 100) \tag{12}$$

The compliance parameter is a dimensionless quantity that measures the degree of deformation of a microchannel wall due to fluid pressure [49,59]. It is defined as:

$$f_p = \frac{1}{72}\left[\frac{W^4(1-\nu)}{hYs^3}\right] \tag{13}$$

where, $W$ is the channel width, $s$ is the undeformed height of the stenosed region, $\nu$ is the Poisson's ratio, $h$ and $Y$ are the thickness and Young's modulus of the top wall.
The compliance parameter is of significant importance in the study of deformable microchannels as it directly influences the pressure-flow characteristics. A higher compliance parameter implies a larger deformation of the wall, resulting in lower hydraulic resistance and a reduced pressure drop across the channel.

## V. EXPERIMENTAL SETUP AND MODEL VALIDATIONS

The validation of the numerical model described in Sec. IV has been conducted through experiments and with the existing numerical and theoretical results from previous works of literature [11,49,54,62]. First, the experimental setup and validation with experimental data are presented. Subsequently, the present numerical model is validated using numerical and theoretical results from previous works of literature [11,49,54,62].

### A. Comparison of Numerical Results with Experimental Data

Fig. 2 shows the experimental setup along with the schematics. The experimental setup comprises two syringe pumps (Unigenetic NE4000 and NE1000) (1 & 2), the test section (microchannel) (3), a microscope (Olympus CKX 53) (4), a pressure sensor (NXP MPX5100DP) (5), an Arduino board (UNO R3) (6), and a data processing system (7). A 10 ml syringe filled with mineral oil is mounted on syringe pump 1 and is connected to the microchannel's primary inlet. Another 10-ml syringe filled with DI water is mounted on syringe pump 2 and is connected to the secondary inlet. As a result, water droplets are generated in the continuous flow of oil into the channel and they flow throughout the main channel. Data from the pressure sensor are collected using an Arduino microcontroller through jumper cables. This comprehensive setup allows for precise control and monitoring of the experimental conditions during droplet generation and migration.

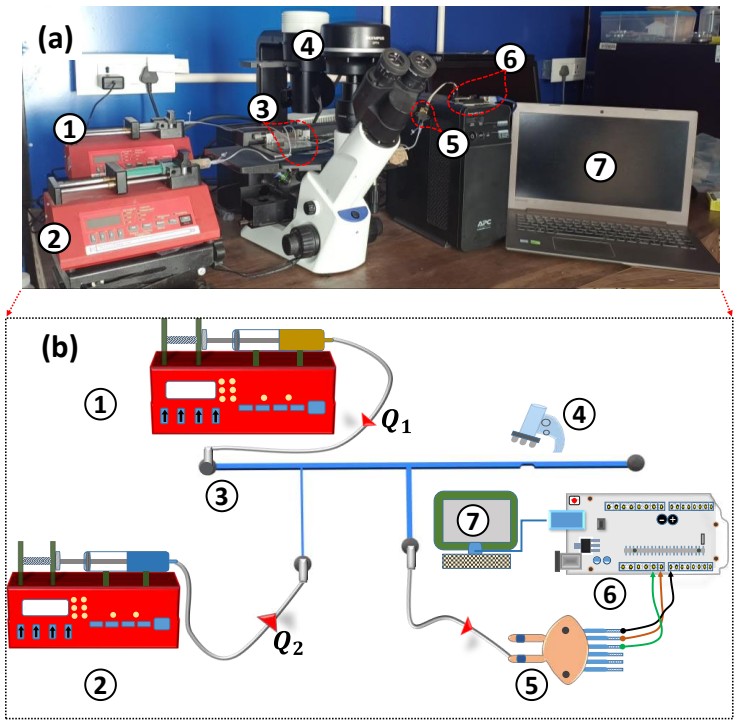


**Fig. 2.** Illustration of (a) the experimental setup and (b) the corresponding schematic of the setup for better visualization.

Fig. 3 shows the fabricated microfluidic device comprising of T-junction droplet generator section and a stenosed microchannel region. The microfluidic device is fabricated using Polydimethylsiloxane (PDMS) material by using a soft-lithography process. First, the mold for the microchannel is fabricated by machining the aluminum sheet using a Micromilling operation with a 0.2 mm diameter tool. Further, Sylgard-184 elastomer is mixed with the curing agent (Dow Corning) in a ratio of 15:1. The mixture is degassed, poured onto the mold with a well, and degassed again to eliminate any trapped air bubbles. Then, the mold with PDMS mixture is cured at a temperature of 90°C for 1 hour. After the curing process, a 1.5-mm biopsy punch is used to create two inlets, pressure, and outlet ports. The PDMS channel is bonded over a clean glass slide using a plasma cleaner (PDC-1, Harrick Plasma, USA). The dimensions of the stenosed channel are measured with an optical microscope (Olympus CKX 53). The microchannel dimensions are shown in Fig. 4. The channel depth and width at the stenosed section are measured to be $500 \pm 15\ \mu m$ & $200 \pm 5\ \mu m$ respectively (Fig. 3a). Also, the length of the stenosed section is $1.4 \pm 0.005\ mm$.

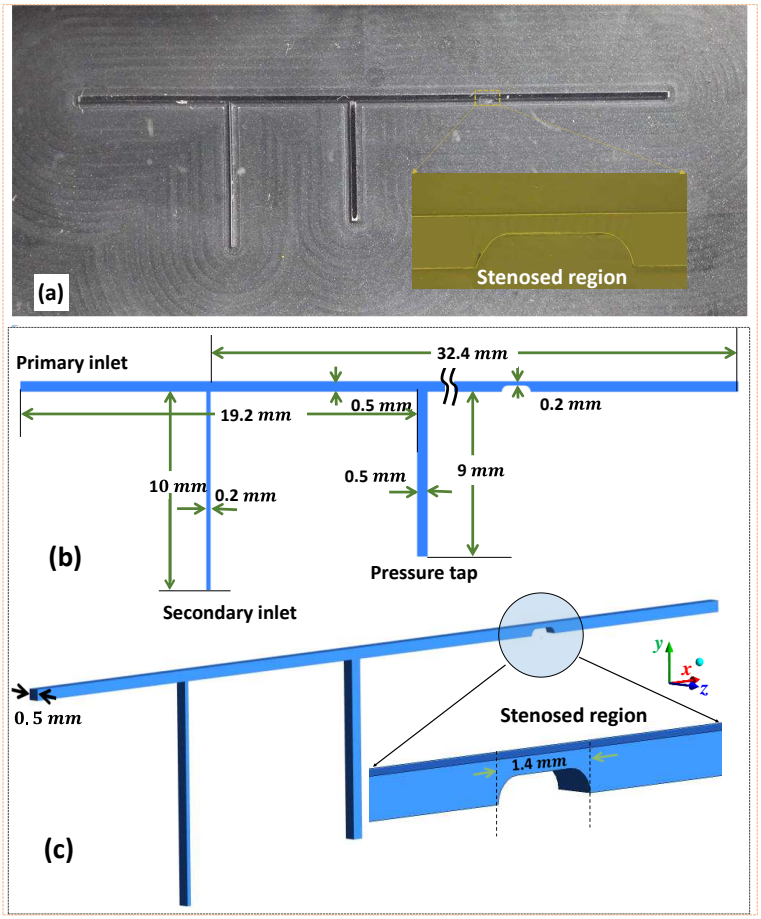


**Fig. 3.** (a) The microscopic image of the model and its schematic with dimensional details; inset shows the zoomed images of stenosed region; (b) the top view schematic and (c) the isometric view schematic.

For the experimentation, the flow rates for both the primary ($Q_1$) and the secondary ($Q_2$) (see Fig. 3(b)) inlets are systematically chosen to initiate droplet generation within the microchannel. An increase in pressure is observed each time a droplet passes through the stenosed region, resulting in a pressure rise recorded by the pressure sensor. This pressure increase, denoted as the critical pressure, is measured through experimental data and compared with the numerical simulation results. The comparison is illustrated in Fig. 4, where the critical pressure data is plotted against the total flow rates ($Q_1 + Q_2$). Please note, here the critical pressure denotes the pressure drop across the stenosed section.

A two-way fluid-structure interaction (FSI) simulation is conducted to further analyze the phenomena, and the critical pressure data from both experiments and simulations are compared. The mesh used in the simulation is dynamically adaptive, with a time step size of 1e-5 s and remeshing length scale ranging from 1e-10 $m$ to 1e-6 $m$. The PDMS channel's stiffness is approximately 1.5 MPa for a base to curing agent ratio of 15:1 [63]. However, in order to save computational cost, for the numerical simulation, the wall stiffness and thickness are selected on the basis of same compliance parameter ($f_p$ =1.8121× $10^{-9}$) i.e., $f_{p_{experimental}} = f_{p_{simulation}}$. The numerical results demonstrate commendable agreement with the experimental data, showing a maximum deviation of less than 15% (Fig. 4). This plot provides a visual representation of the pressure drop as a function of varying flow rates, offering insights into the dynamic relationship between fluid dynamics and the stenosed region within the deformable microchannel. To ensure the reliability of the results, each experiment is repeated thrice.

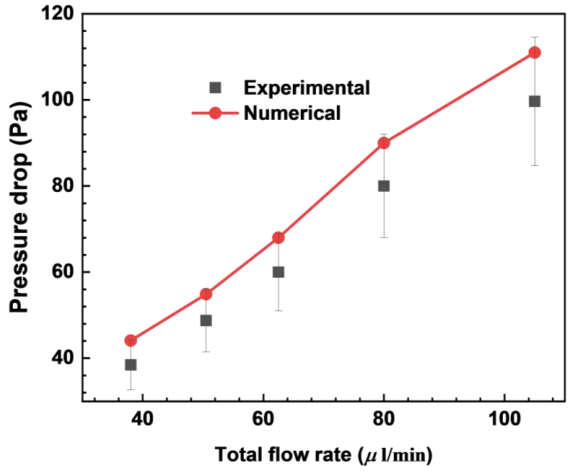


**Fig. 4.** Comparison of experimentally obtained pressure drop values with the values obtained through simulation at different total flow rates ($Q_1 + Q_2$).

### B. Model Validation with Existing Studies and Mesh Independence Test

The pressure drop across a simple, 3D microchannel with a compliant top wall [49] is used for the validation of the numerical methodology adopted for fluid-solid interaction (FSI). The validation with the experimental and theoretical data of Raj et al. [49], theoretical data of Christov et al. [62], and numerical results of Shidhore et al. [54] is shown in Fig. 5 (a). At low flow rates, the present numerical results match well with all the theoretical data [49,62] and numerical results of Shidhore et al. [54]. However, the present numerical results are in better

agreement with the experimental data of Raj et al. [49] than the results of Shidhore et al. [54], at all flow rates, with a maximum deviation being well within 10%.

Another validation test has been carried out for the volume of fluid (VOF) model used in this study. The geometry used is a droplet passing through a rigid confinement [11]. The present simulation results match well with the theoretical and numerical works of Zhang et al. [11], as shown in Fig. 5 (b). The current simulations align closely with theoretical model of Zhang et al. [11], with deviations within ±14% across all flow rates, as shown in Fig. 5 b. The discrepancy in pressure drop is primarily due to the omission of shear force as noted in Ref. [64], and could also be due to the omission of the entry and exit losses in theoretical modeling. These errors becomes more pronounced at higher flow rates, highlighting the significance of shear force [64]. As a result, pressure drop deviations increase notably with rising flow rates compared to Zhang et al. theoretical predictions [11].

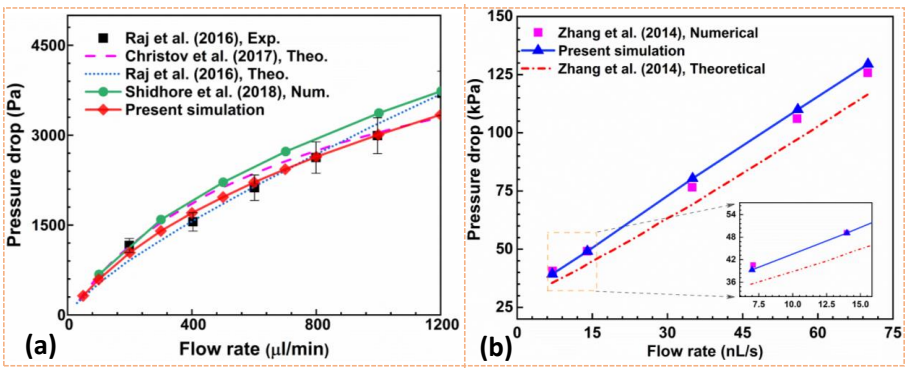


**Fig. 5.** Validation of (a) FSI model in terms of pressure drop across the channel at different flow rates. (b) VOF model in terms of pressure drop relationship with flow rates. The error bars shown in the left figure is ±10% with respect to the experimental results of Raj et al. [49].

The problem for this study, as discussed in Sec. VI, has been the investigation of a droplet through a deformable stenosed channel. Before performing the parametric study to understand the blockage phenomena, a mesh independence study has been carried out and shown in Fig. 6. The different mesh size considered is shown on the abscissa. The time during which the pressure across the stenosed portion (planes at $x = 25\ \mu m$ and $x = 375\ \mu m$, see Fig. 1) is maximum as the droplet moves through it is denoted by $t_{cr}$. The corresponding pressure drop is denoted by $\Delta p_{t_{cr}}$. The value of $\Delta p_{t_{cr}}$ starts converging after 148040 numbers of cells. Fig. 6 (b) shows the pressure profile at the midpoint of the stenosed region with respect to the flow time. The domain with 148040 number cells closely matches the model with the finest mesh. So, all the simulations in this study are performed using 148040 cells which have a maximum deviation of 0.015% in $\Delta p_{t_{cr}}$ with respect to the finest mesh.

Furthermore, the simulation incorporates the dynamic mesh technique, including smoothing and remeshing methods, to proficiently replicate the dynamic behaviour of walls. This approach ensures a sufficient cell density in proximity to the boundaries, a critical factor for precisely depicting the creation of lubrication films. The mesh deformation is based on the smoothing method, which uses a diffusion technique with a boundary-distance function to preserve the mesh quality near the boundaries. The diffusion parameter is set to 2, which controls the rate of mesh deformation. The mesh adaptation is performed using the remeshing methods, which create or delete cells according to the local mesh size and quality criteria. The remeshing methods used in this study are local-cell, local-face, and region-face, which operate on different regions of the mesh. The remeshing interval is set to 1, which means the remeshing is done at every time step. The same approach is used while validating the FSI model, which is

independent of the mesh size. So, it can be concluded that the dynamic mesh approach is also independent of the mesh size.

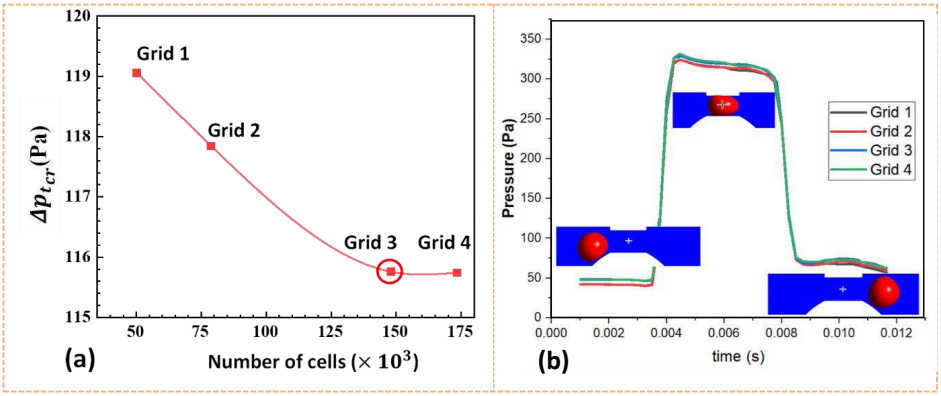


**Fig. 6.** Grid independence test: (a) The pressure drop at $t_{cr}$ across the channel at different mesh element sizes, and (b) Pressure variation at the central point (shown with crosshair symbol) of the stenosed region.

## VI. RESULTS AND DISCUSSION

The droplet migration in the stenosed channel is divided into four stages: (A) entry, (B) passage, (C) exit, and (D) relaxation [33]. Out of these stages, understanding the entry and passage (explained in the following subsections) is crucial with respect to the objective of the present study, i.e., to understand and predict blockages in microchannels.

### A. Entry

In this stage, the droplet enters the stenosed region from its left side (see Fig. 1). The entry process plays an important role in microfluidics, for example, the entry process of blood cells through a stenosed channel is an important factor in developing and treating cardiovascular diseases such as stroke [65]. In the following subsection, we investigate the effect of the physical and geometrical properties on the entry process.

*A.1. Effect of physical properties on the droplet entry process:*

The effect of non-dimensional quantities introduced in Sec. IV such as viscosity ratio ($\mu^*$), surface tension ratio ($\sigma^*$) and density ratio ($\rho^*$ ) on the droplet entry process are studied in this subsection. First, the viscosity ratio ($\mu^*$), is varied ($0.1 \leq \mu^* \leq 4$) at surface tension ratio, $\sigma^* = 125$, density ratio, $\rho^* = 1$, diameter ratio, $D^* = 1.35$, and stiffness ratio, $Y^* = 1$ ($f_p = 8.14862 \times 10^{-7}$). Next, the effect of $\sigma^*$ is studied ($25 \leq \sigma^* \leq 500$), at $\mu^* = 4$, $\rho^* = 1$, $D^* = 1.35$, and $Y^* = 1$. Further, the effect of density ratio, $\rho^*$ is analysed in the range; $0.4 \leq \rho^* \leq 1.5$, with $\mu^* = 4, \sigma^* = 500$, $D^* = 1.35$, and $Y^* = 1$.

*A.1.1 Effect of Viscosity ratio ($\boldsymbol{\mu^*}$)*

Viscosity, defined as a fluid's resistance to flow due to internal friction between its molecules, significantly influences the entry process, as illustrated in Fig. 7. In each subfigure (Fig. 7 (a-i)), pressure contour along the flow direction and the wall shear stress ($WSS$) contour on the top surface of the stenosed wall are shown at the upper and lower parts, respectively. Both the contours are plotted for three different positions during the droplet's entry process at three different viscosity ratios. As $\mu_d$ increases, viscosity ratio increases, the droplet's resistance to deformation within the stenosed channel rises, leading to increased internal pressure (viscosity-induced pressure) as depicted in the pressure contours of Fig. 7. The deformed droplet, with excess internal pressure, applies pressure on the wall along its contact line, resulting in resistance force from the wall against droplet motion. Additionally, increasing $\mu^*$ corresponds to increased $WSS$ (see Fig. 7), further augmenting resistive force acting on the droplet. These combined factors contribute to an exponential rise in entry time ($t_e$ ) with increasing $\mu^*$,as depicted in Fig. 8 (a) (Multimedia view). Additionally, in the following paragraph, the effect of $\mu^*$ on $t_e$ is explained using the concept of Capillary number.

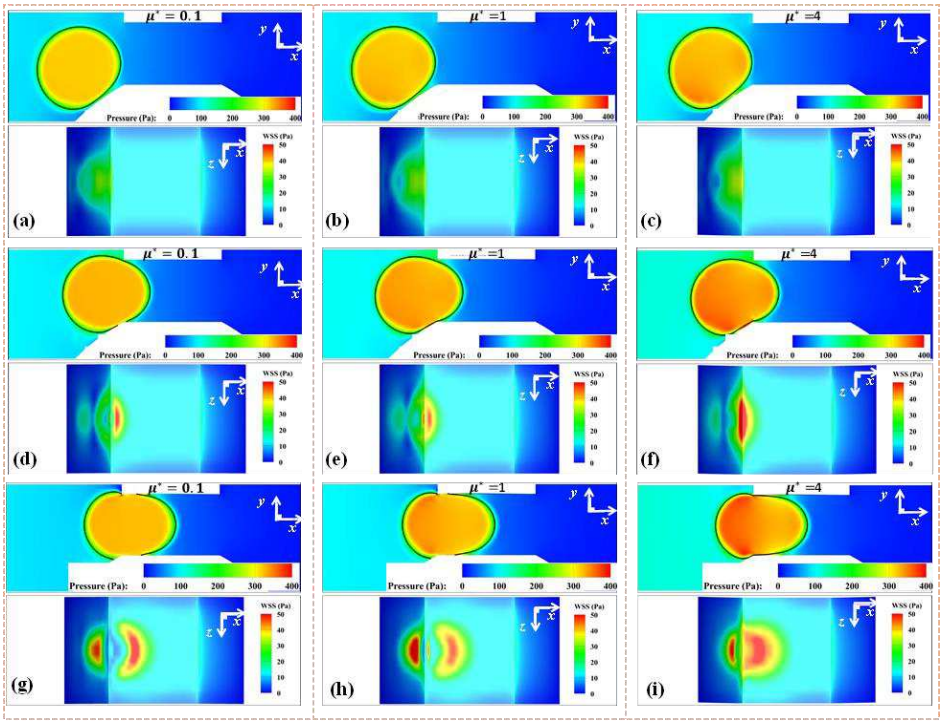


**Fig. 7.** Pressure along the flow direction ($xy$-plane) and wall shear stress ($WSS$) at the same instant on the top surface ($xz$-plane) of the stenosed wall shown, respectively, on the top and bottom of each figure (a-i). The two contours are for three different positions of the droplet during the entry, respectively, for $\mu^* = 0.1, 1,$ and 4.

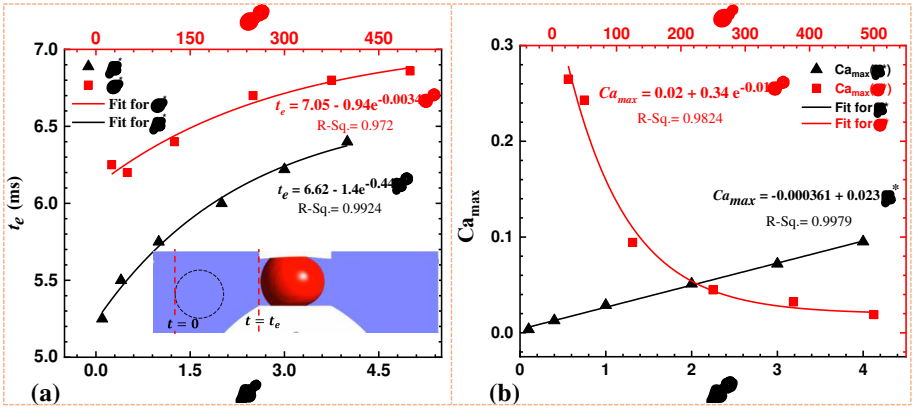


**Fig. 8.** Plots showing (a) the effect of the viscosity and the surface tension on the droplet's entry time with a schematic (shown in inset) exhibiting the definition of the entry time, $t_e$ (Multimedia view) and (b) Capillary number variation considered for analysing the effect of the viscosity and the surface tension ratios on the droplet migration.

The Capillary number is an important parameter that influences droplet migration through stenosed regions. A low capillary number means that the interfacial tension forces dominate over the viscous forces, leading to droplet shapes being spherical to a larger extent. On the other hand, a high capillary number means that the viscous forces dominate over the interfacial tension forces, leading to droplets with a more elongated shape. The velocity considered here for defining the capillary number (see Eq. 11) is the maximum velocity during the entry process, and therefore it is denoted by $Ca_{max}$ in Fig. 8 (b) which shows that $Ca_{max}$ increases linearly with $\mu^*$. At lower values of $\mu^*$, the capillary number tends to zero, which means that the effect of the viscous forces is negligible, and only the interfacial tension opposes the droplet movement. Therefore, the droplet enters with less resistance leading to a smaller entry time at lower $\mu^*$ values. On the other hand, at a higher $\mu^*$, i.e., at higher capillary numbers, viscous forces dominate inside the droplet leading to a larger entry time, as explained earlier.

Although the pressure inside the droplet and the $WSS$ is high (see Fig. 7) and $Ca_{max}$ is linearly increasing for the largest $\mu^* = 4$ considered, the entry time curve in Fig.8 (a) tends to flatten at $\mu^* = 4$. This is because a thin lubrication film develops at higher $\mu^*$ (see Fig. 7 (i)), which facilitates droplet entry [17]. The smoother entry process with the increasing $\mu^*$ values is explained with the help of streamlines in Appendix A. The shape of the trailing end (towards the upstream of the entry in the stenosed region) of the droplet also changes with the increase in $\mu^*$, as seen in Fig. 7 (g-i). The evolved shape actually helps in the smooth transition of the droplet into the stenosed region. As, $\mu^*$ increases the lubrication film thickens and the entry process smoothens. This leads to a decrease in the increasing rate of $t_e$ with $\mu^*$.

*A.1.2 Surface tension ratio, $\boldsymbol{\sigma^*}$*

Surface tension (or interfacial tension) is a force that causes a droplet to resist deformation by reducing its surface area [66]. When the surface tension of a droplet exceeds that of the surrounding fluid (0.005 N/m), it induces a capillary force that draws the droplet towards the walls of the microchannel. This attraction causes the droplet to adhere more strongly to the walls, especially in stenotic regions where the flow is already constricted. This effect is evident in the various droplet shapes observed at different values of $\sigma^*$ in Fig. 9. As $\sigma^*$ increases, the droplet's

resistance to changing its shape also increases, leading to a rise in $WSS$ as the contact line of the droplet with the wall expands. Additionally, from Fig. 9, it is apparent that the pressure inside the droplet increases as the surface tension increases. This pressure buildup is attributed to the compression of the droplet by molecules on its surface, which seeks to maintain a minimal surface area to counterbalance the surface tension force. At the depicted time instant in Fig. 9, the developed pressure inside the droplet is minimal at $\sigma^* = 25$ ($\sim 150\ Pa$), while it is maximal at $\sigma^* = 500$ ($\sim 1130\ Pa$).

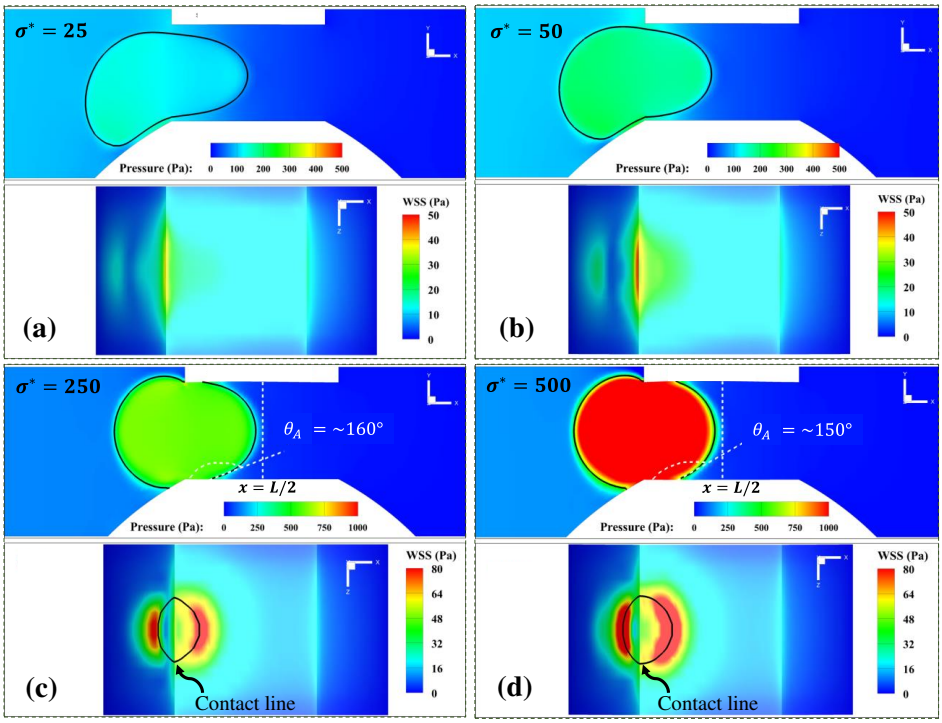


**Fig. 9.** Contours for pressure along the flow direction ($xy$-plane) and the wall shear stress at the same instant on the top surface ($xz$-plane) of the stenosed wall for (a) $\sigma^* = 25$, (b) $\sigma^* = 50$, (c) $\sigma^* = 250$ and (d) $\sigma^* = 500$. Advancing contact angle ($\theta_A$) of the droplet, when its tip is about to cross the centre ($x = L/2$) of the stenosed wall and the contact line developed by the droplet on the top surface of the stenosed wall is also shown for $\sigma^* = 250$ and $\sigma^* = 500$. The legends for pressure and $WSS$ for $\sigma^* = 250$ and 500 are different than that of $\sigma^* = 25$ and 50, for the sake of proper quantitative representation. Pressure contours along with the streamlines (droplet-relative reference frame) for the surface tension ratios during the entry process is shown in Appendix B, Fig. 31.

At lower $\sigma^*$ values ($\leq 125$), such as $\sigma^* = 25$ and $\sigma^* = 50$ as depicted in Fig. 10 (a-b), the droplet remains physically separated from the stenosed region. This separation allows for the presence of a continuous phase layer between the droplet and the channel walls, facilitating a smooth, contactless entry process. However, as $\sigma^*$ increases, the film between the droplet and the walls begins to attenuate. Significant contact between the droplet and the walls occurs for $\sigma^*$ values $\geq 150$, illustrated in Fig. 9 (c-d) for $\sigma^* = 250$ and $\sigma^* = 500$. In Fig. 9 (c-d), in addition to the contact line displayed on the top surface of the stenosed wall, the advancing contact angle ($\theta_A$, a

measure of droplet spreading on a surface) is shown to elucidate the increased adherence to the wall with higher surface tension. It is observed that $\theta_A$ decreases with increasing $\sigma^*$ for $\sigma^* = 250$ and $\sigma^* = 500$, indicating greater droplet adherence to the stenosed wall. A droplet with higher $\sigma^*$ exerts more pressure on its surroundings, whether on the channel walls or at the front tip. The top wall, being thinner and more sensitive to deformation than the stenosed wall, undergoes more deformation, pulling droplet volume towards the curvature developed on the top wall. Consequently, the advancing contact angle decreases with increasing $\sigma^*$.

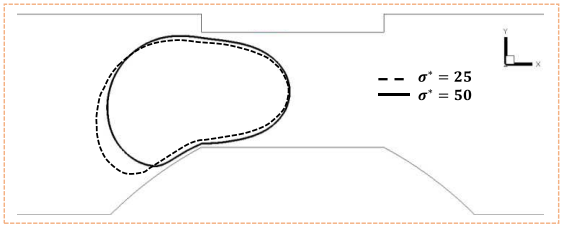


**Fig. 10.** The spreading area is more for the droplets with $\sigma^* = 25$ than the droplet with $\sigma^* = 50$.

The effect $\sigma^*$on the droplet entry time for exponentially decaying Capillary number (see Fig. 8 (b)) is shown in Fig. 8 (a). The above factors lead to an exponential increase of $t_e$ with respect to $\sigma^*$. However, at much lower values of $\sigma^*$, the trend is different. The $t_e$ at $\sigma^* = 50$ is slightly less than that at $\sigma^* = 25$. A droplet with low interfacial tension has weaker cohesive forces among its molecules, resulting in a greater tendency to spread out on a surface, as shown in Fig. 10. The spreading at such lower surface tension delays the entry process that we observe in Fig. 9, where $t_e$ is slightly more for $\sigma^* = 25$ than for $\sigma^* = 50$, as seen in Fig. 8 (a). Capillary number decays exponentially, and it asymptotes at higher values of $\sigma^*$, as shown in Fig. 8 (b). The asymptotic behavior at higher values of $\sigma^*$ indicates the dominance of surface tension forces over the viscous forces at high values of $\sigma^*$. The formation of the lubrication films shows an interesting relationship with the Capillary number. It is observed that a lubrication film always exists between the droplet and the wall for $Ca_{max} \geq 0.095$.

*A.1.3 Density ratio,* $\boldsymbol{\rho^*}$

Lastly, among the droplet properties, the impact of density ratio ($\rho^*$) on the droplet entry process is examined. Fig. 11 illustrates this effect at three distinct time points ($t_1 < t_2 < t_3$), comparing droplets with $\rho^*$ values of 0.4 (depicted by dashed lines) and 1.2 (depicted by solid lines). Initially, at the onset of flow, the positions of the two droplets nearly coincide, indicating minimal influence from density or inertia, as shown in Fig. 11 (a). However, as the droplet approaches and collides with the stenosed region, the inertial effect becomes more pronounced. The droplet with $\rho^* = 1.2$ experiences greater inertia due to its higher density, resulting in it being pushed further into the stenosed region compared to the droplet with a lower density ratio ($\rho^* = 0.4$), leading to a delayed entry for the latter. This distinction is evident in Fig. 12, where the entry time decreases linearly with an increase in density ratio, further supporting the observed trends.

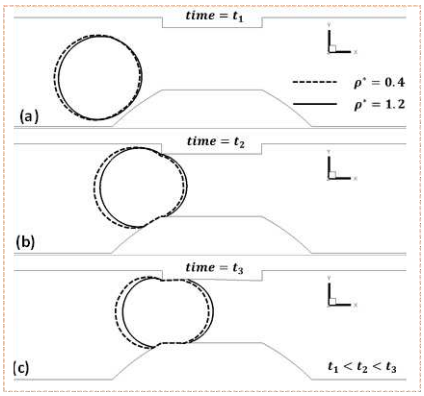


**Fig. 11**. Role of density ratio in droplet's entry process. The dashed and solid lines are for $\rho^* = 0.4$ and $\rho^* = 1.2$, respectively at the time, (a) $t_1$, (b) $t_2$, and (c) $t_3$.

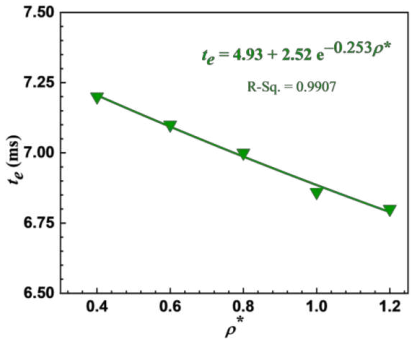


**Fig. 12.** Effect of density on the droplet's entry time.

*A.2. Effect of droplet geometry on the droplet entrance time*

After analysing the effect of fluid property, we see the effect of droplet diameter ratio ($D^* = D/s$) on the entrance time. This will enable us to understand the role of droplet size in building pressure across the constriction leading to cardiovascular diseases like stroke. The diameter ratio differs in the range; $0.87 \leq D^* \leq 1.35$ at $\mu^* = 4$, $\sigma^* = 500$, $\rho^* = 1$, and $Y^* = 1$. As the diameter decreases, the pressure inside the droplet increases (as Laplace pressure $\propto 1/\mathrm{D}$), and the same is shown in Fig. 13. However, at lower diameter ($D < s$), the droplet moves without any such hindrance in the stenosed region and therefore entry time is less as can be seen in Fig. 14. On the other hand, if the size increases ($D > s$) the pressure building in the droplet diminishes, but since the droplet comes in contact with the walls of the stenosed region, it leads to hindrance to the flow resulting in more pressure drop across the stenosed region. This leads to an increase in the entry time, as shown in Fig. 14. The entry time, $t_e$ has a linear relationship with the normalised diameter $D^*$. We can also observe (see bottom of Fig. 13 a-b) that as the droplet with a larger diameter comes in contact with the walls of the stenosed region, WSS increases, leading to more resistance.

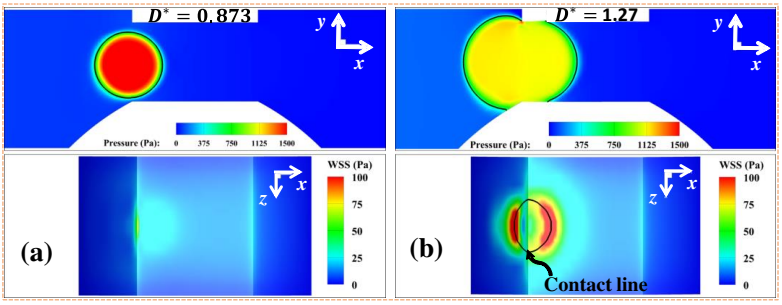


**Fig. 13.** Contours for pressure along the flow direction (*xy*-plane) and the *WSS* at the same instant on the top surface (*xz*-plane) of the stenosed wall for (a) $D^* = 0.873$, and (b) $D^* = 1.27$.

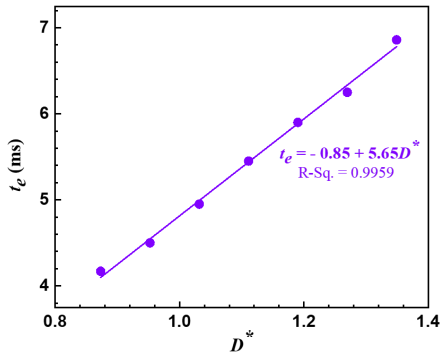


**Fig. 14.** The entry time ($t_e$) has a linear relationship with the normalised diameter ($D^*$).

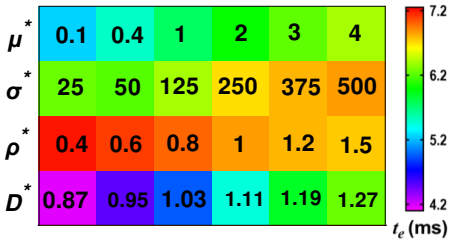


**Fig. 15.** Colour map conjointly showing the effect of different fluid properties (viscosity, surface tension, and density) and the diameter on the droplet's entry time.

To summarise the effect of the three fluid properties and the diameter ratio on the droplet's entry time, a colour map is plotted in Fig. 15. From the map, one can easily conclude, based on the colour contrast, that the effect of the density on the entry time is more significant. However, among the droplet's physical properties and for $D^* > 1$, the effect of the viscosity and the surface tension on the entry time is more significant than density.

### B. Passage

As mentioned earlier, apart from the entry process, the droplet passage through the stenosed region also plays a critical role in blockages. During passage, the droplet continues to move through the stenosed region. The passage stage is characterized by the interaction between the droplet and the walls of the stenosed channel. The properties of the droplet and continuous phase (viscosity, surface tension, and density), and the size of the droplet all influence the dynamics of the passage process and are considered in this subsection.

As the viscosity ratio ($\mu^*$) increases, both the pressure within the channel and inside the droplet rise, as illustrated in Fig. 16. The elevation in channel pressure arises from increase in viscous resistance, while pressure buildup inside the droplet is due to the resistance it encounters as droplet squeezes between the walls of the constricted region. Notably, the pressure within a droplet may not surpass that outside solely due to surface tension (i.e., Laplace pressure). Viscosity also plays a role in influencing droplet pressure upon entering a stenosed region, as depicted in Fig. 7. For $\mu^*$ values of 0.1 and 1, the droplet maintains contact with the stenosed region, as evidenced by the contact line drawn on the top surface of the stenosed wall in Fig. 16 (a-b). However, as $\mu^*$ increases, droplet contact diminishes and disappears entirely at higher $\mu^*$ due to the development of a lubrication film between the droplet and the wall, consistent with observations during the entry process in Sec. VI A.1.1. This disappearance of contact is evident at $\mu^* = 4$, as shown in Fig. 16 (c). Furthermore, Fig. 16 (d) presents a cross-sectional view of pressure contours for various viscosity ratios, providing additional insights into the pressure distribution within the channel and droplet. The increasing pressure trend with increase in $\mu^*$ can be further witnessed in Fig. 16 (d).

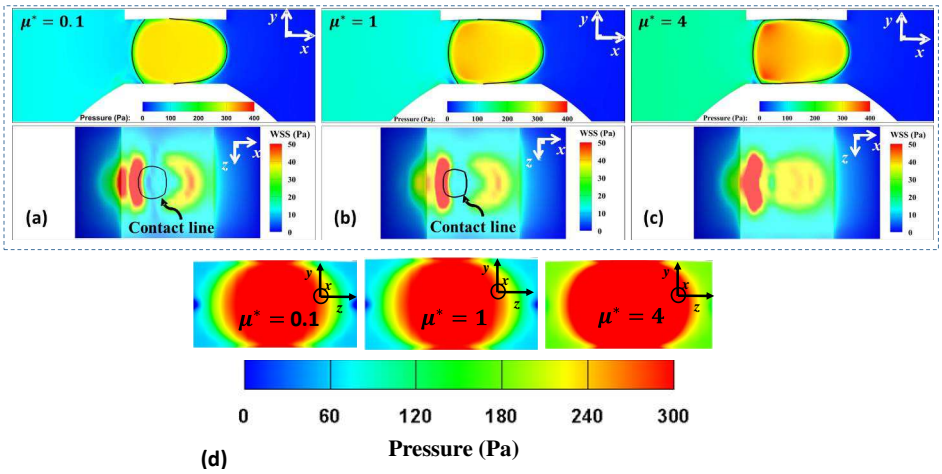


**Fig. 16.** Contours for pressure along the flow direction ($xy$-plane) and the $WSS$ at the same instant on the top surface ($xz$-plane) of the stenosed wall for (a) $\mu^* = 0.1$, (b) $\mu^* = 1$, and (c) $\mu^* = 4$. (d) Pressure contours along y-z plane.

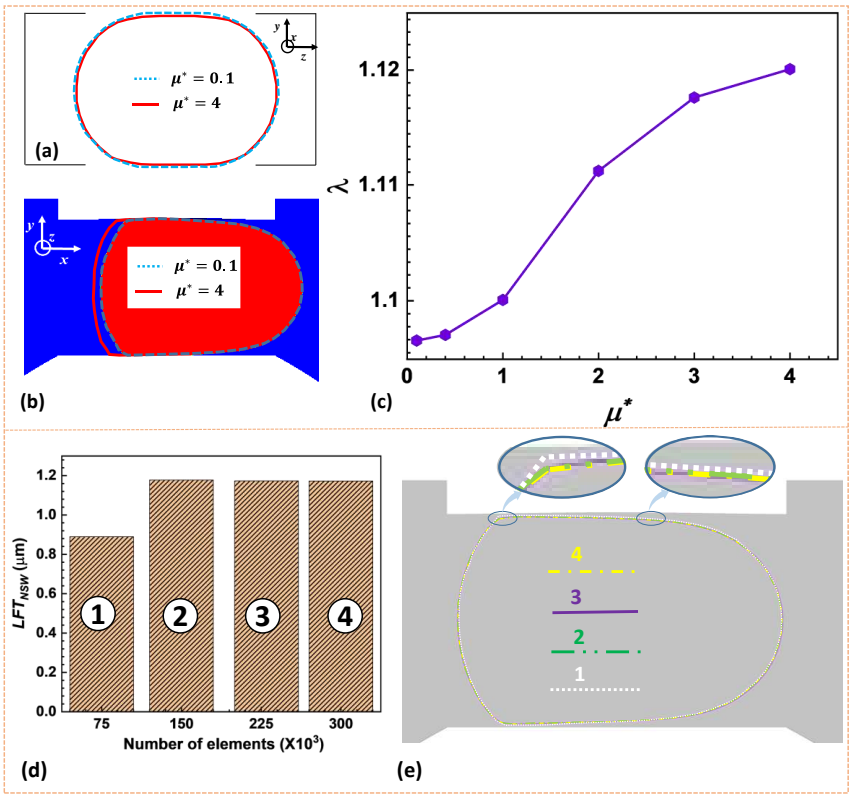


**Fig. 17**. The volume fraction isoline ($\phi_w = 0.5$) plot in (a) y-z plane, i.e., across the flow direction and (b) x-y plane i.e., along flow direction for $\mu^* = 0.1$ and 4. (c) The elongation ratio ($\lambda = l_e/D$) plot with respect to viscosity ratio. Grid sensitivity test for the lubrication film thickness: (d) lubrication film thickness at near the non-stenosed wall ($LFT_{NSW}$) at different numbers of mesh elements, and (e) the volume fraction isoline ($\phi_w = 0.5$) for the respective element size.

The existence of the lubrication film can also be witnessed from the volume fraction isoline ($\phi_w = 0.5$) plot in y-z plane for $\mu^* = 0.1$ and 4, as shown in Fig. 17 (a). The droplet gets squeezed across the flow direction, due to the presence of the lubrication layer between the droplet and the stenosed region [2]. To conserve its volume, a droplet with higher viscosity gets elongated along the flow direction, which can be seen in Fig. 17 (b). The elongation along the flow direction ($xy$ plane) is represented using the elongation ratio ($\lambda$), defined as the ratio of length along the flow direction ($l_e$) to the original diameter ($D$) of the droplet. With the increase in viscosity ratio, the lubrication layer develops, the droplet elongates along the flow direction, and hence, the elongation ratio increases with the increase in viscosity ratio, as can be seen in Fig. 17 (c). The presence of a lubrication layer reduces the recirculation zone developed due to droplet -wall contact in the stenosed region, as shown in Appendix C. The streamlines drawn inside the droplet, help in understanding the smoother passage at higher values of $\mu^*$ (Appendix D). Further, it is observed that with the increase in the viscosity ratio, the thickness of the lubrication film is more in the vicinity of

the non-stenosed wall as compared to the stenosed wall, as depicted in Fig. 18 (a). In addition to the mesh-independent study concerning critical pressure (see Sec. V B), a grid sensitivity analysis was conducted for Lubrication Film Thickness ($LFT$) for cases where the lubrication film was observed. Fig. 18 (d-e) illustrates the results, showcasing $LFT$ near the non-stenosed wall ($LFT_{NSW}$) at various mesh element numbers and the volume fraction isoline ($\phi_w = 0.5$) for corresponding element sizes. The element size of 148040, coupled with the dynamically adaptive mesh, proves to be adequate for capturing $LFT$ in the proximity of the channel walls as well as the pressure drop across the stenosed channel (see Sec. V B). This analysis confirms the independence of the presented $LFT$ results from the mesh size, reinforcing the robustness and reliability of the findings. The bottom of Fig. 16 (a-c) shows the $WSS$ contour. It can be observed that the $WSS$ is the least for $\mu^* = 1$, due to the negligible shear resistance between the two phases. And it is highest for $\mu^* = 4$ despite the formation of the lubrication film. This is due to the high resistance experienced by the continuous phase layer beneath the droplet because of the higher viscosity difference. However, the increased $WSS$ does not indicate increased resistance to the droplet motion, as can be seen in Fig. 19. The droplet velocity throttles at $\mu^* \geq 3$, and it does not decrease further due to the lubrication film between the droplet and the channel wall, which can also be manifested from the passing time ($t_p$) plotted in Fig. 18 (c). The passing time is the time that the droplet takes to pass through the stenosed portion completely.

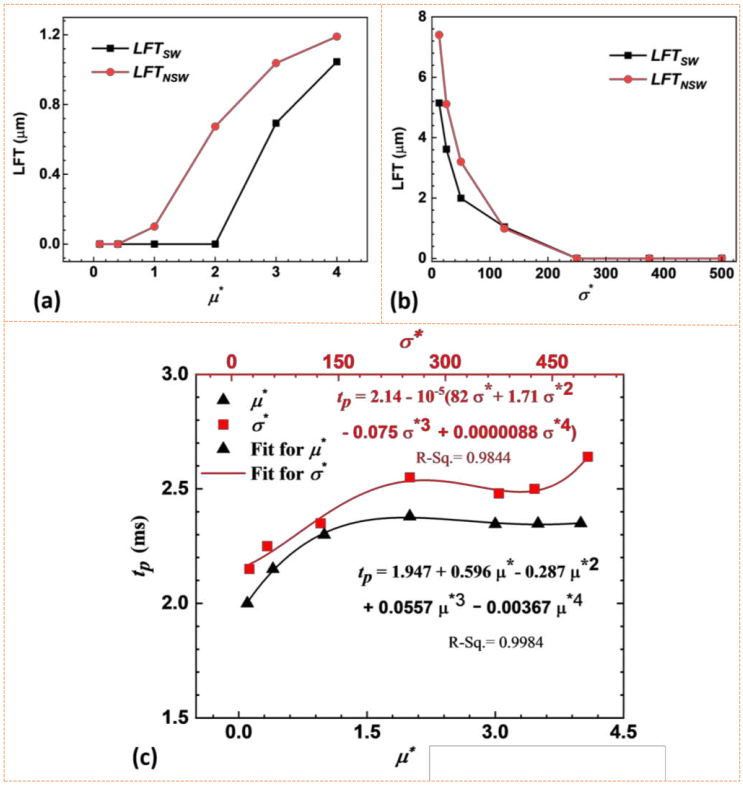

**Fig. 18.** Lubrication film thickness ($LFT$) in the vicinity of the stenosed and non-stenosed wall at different (a) viscosity and (b) surface tension ratios. (c) Effect of viscosity and surface tension ratios on droplet's passing time ($t_p$).

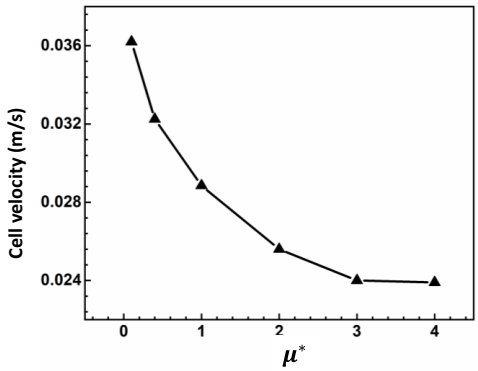


**Fig. 19.** Effect of $\mu^*$ on the droplet velocity during the passage process.

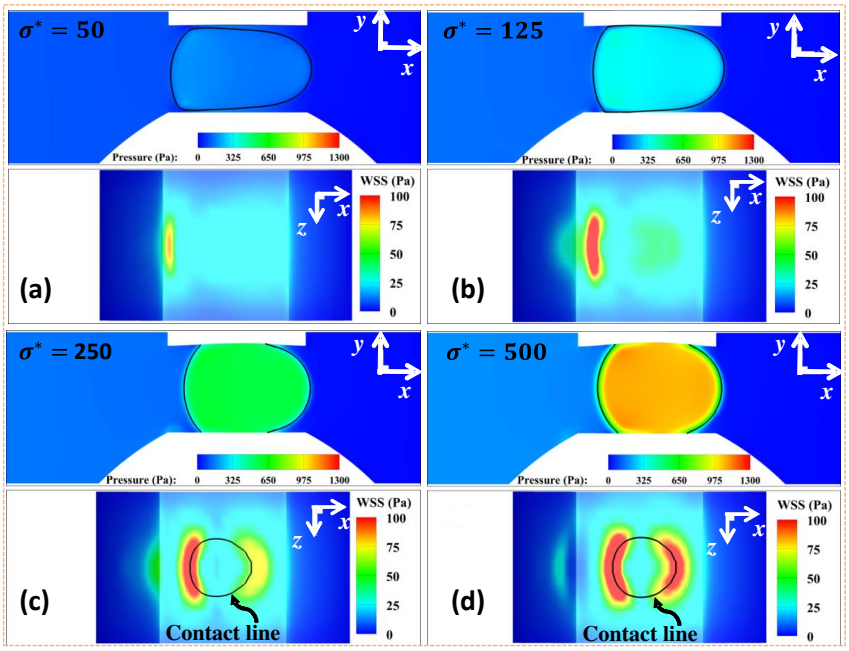


**Fig. 20.** Contours for pressure along the flow direction ($xy$-plane) and the $WSS$ at the same instant on the top surface ($xz$-plane) of the stenosed wall for (a) $\sigma^* = 50$, (b) $\sigma^* = 125$, (c) $\sigma^* = 250$, and (d) $\sigma^* = 500$. Pressure contours

and streamlines (droplet-relative reference frame) for various surface tension ratios during passage is shown in Appendix E, Fig. 34.

With the increase in surface tension, the pressure inside the droplet increases substantially, as depicted in Fig. 20. At lower values of $\sigma^*$, a continuous phase layer is always there between the droplet and the channel wall (see Fig. 18(a-b)), as was seen earlier during the entry phase. A higher magnitude of $LFT$ can be seen at lower $\sigma^*$ values in Fig. 20 (b). However, for $\sigma^* > 125$, the pressure development inside the droplet is enough for the droplet to push the channel wall, and so we observe a vanishing lubrication layer with the increase in $\sigma^*$values (see Fig. 20 (b)). In other words, we can say that the wall adherence of the droplet increases with the increase in $\sigma^*$, which resists the droplet movement in the stenosed region. The increasing resistance by the stenosed wall with an increase in $\sigma^*$ can be observed in the $WSS$ contours, as shown in the bottom of Fig. 20(a-d). Fig. 20 (c) shows the effect of $\sigma^*$ on $t_p$. It increases till $\sigma^* = 250$, then decreases at $\sigma^* = 375$, and again increases. The initial increment is due to the building up of hindrance as the droplet starts attaining a more spherical shape due to an increase in pressure inside the droplet. Further, it decreases at $\sigma^* = 375$, as the deformed wall or the increased cross-sectional area facilitates easy passage of the droplet. However, the increased cross section brings in the curvature effect, where the droplet gets an opposing force from the curved portion of the deformed wall, leading to an increase in $t_p$.

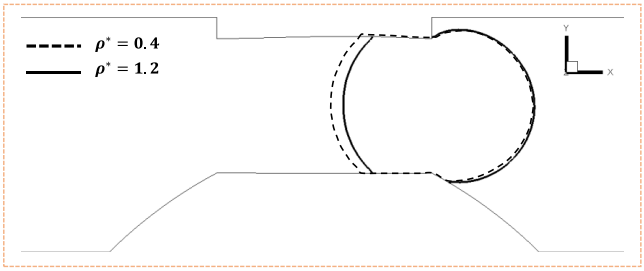


**Fig. 21.** Role of density ratio on the droplet's passage process. The dashed and solid lines are for $\rho^* = 0.4$ and $\rho^* = 1.2$, at a particular time instant ($t = 10.25\ ms$).

The effect of density and diameter ratios on the passage process has also been investigated. Fig. 21 shows the droplet position at a particular time instant for $\rho^* = 0.4$ and $\rho^* = 1.2$. In Sec. VI A.1.3, the effect of density on the entry process is discussed, where the inertial effect has played a dominating role in pushing the droplet of higher density into the stenosed region (see Fig. 11). So, we observed a lesser entry time for $\rho^* = 1.2$ (see Fig. 12). However, when the droplet is at the end of the passing stage, the effect of inertia starts diminishing, as can be seen in Fig. 20. The two droplets are almost at the same position at $t = 10.25\ ms$. So, one can conclude that the passing process, unlike the entry process, is dominated by the rising pressure inside the droplet. The increasing pressure and $WSS$ with $\rho^*$ can be witnessed in the pressure and $WSS$ contours for different values of $\rho^*$, as shown in Appendix F, Fig. 35.

The effect of diameter on the passage process is similar to what we observed in its effect on the entry process. So, for the sake of brevity, the pressure and the $WSS$ contours have been kept in Appendix G, Fig. 36.

### C. Comparison of hydrodynamic resistance ($R$) in deformable stenosed and non-stenosed microchannel.

The hydrodynamic resistance ($R = \Delta p_{t_{cr}}/Q$) in the stenosed channel is compared with that of the non-stenosed channel in this subsection. This will help in understanding how different properties influence the flow resistance in a stenosed channel and to contrast the same with a normal (non-stenosed) channel.

Fig. 22 (a) and (b) show the comparison between the hydrodynamic resistance ($R$) experienced by the droplet while passing through the stenosed and the non-stenosed microchannel for varying $\mu^*$ and $\sigma^*$. The hydrodynamic resistance for stenosed channels increases with viscosity as the droplet brings hindrance to the flow due to its increased flow reluctance, as explained in Sec. VI A and B. While the effect of viscosity remains negligible for non-stenosed channels. The plot for the total maximum deformation of the wall is shown in Fig. 23 (a) and (b), respectively for the variations of $\mu^*$and $\sigma^*$. The wall deformation changes very little with the change in $\mu^*$ as compared to the change in $\sigma^*$. This is due to less pressure rising inside the channel with a change in $\mu^*$ values (see Fig. 8) as compared to the pressure rise with a change in $\sigma^*$ values.

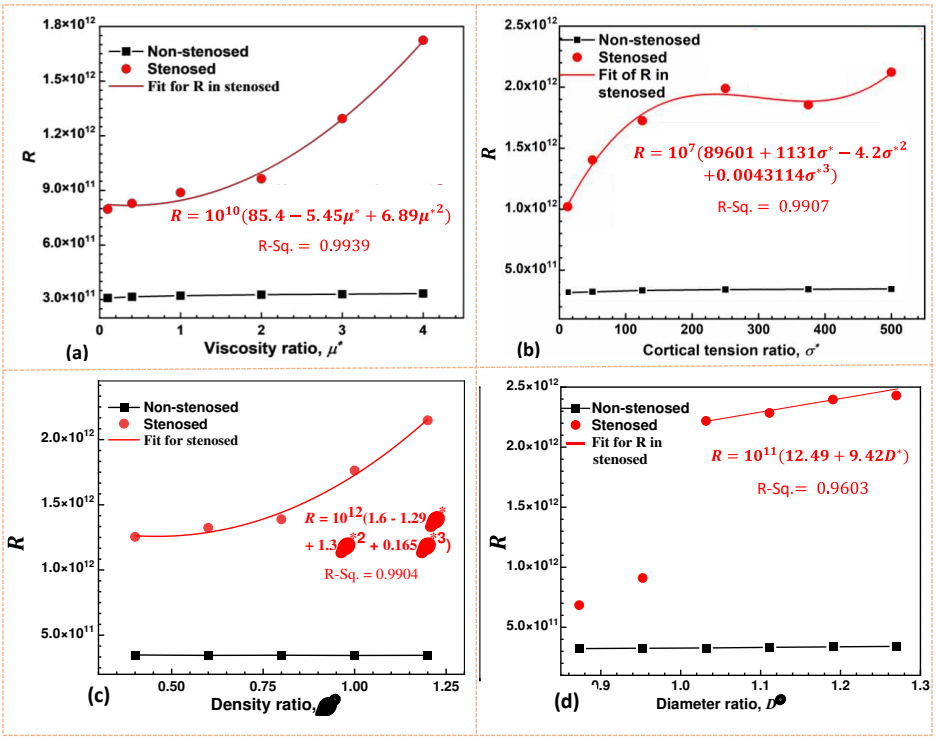


**Fig. 22.** Comparison of hydrodynamic resistance ($R$) in stenosed channel to that of non-stenosed channel with different properties: (a) viscosity, (b) surface tension, (c) density, and (d) diameter.

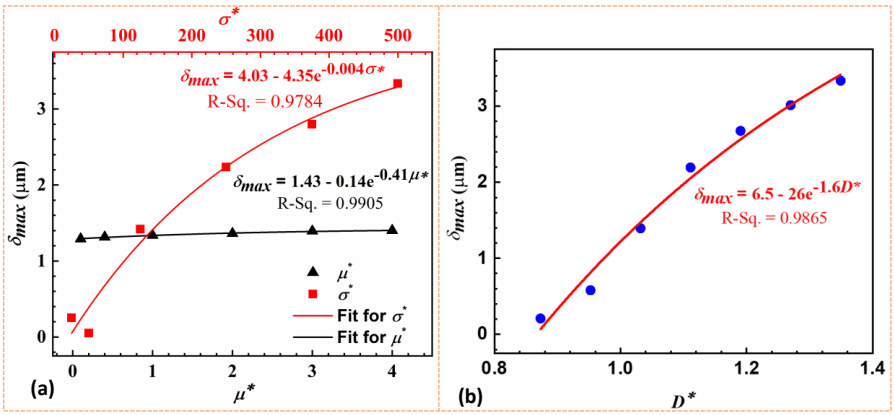


**Fig. 23.** The effect of (a) viscosity ratios $\mu^*$ and surface tension ratios $\sigma^*$, and (b) diameter ratios $D^*$ on the total maximum deformation of the stenosed wall.

As surface tension rises, resistance escalates until reaching $\sigma^* = 250$, after which it gradually declines until $\sigma^* = 375$. Subsequently, there is a slight upward trend, as illustrated in Figure 22 (b). According to the Laplace equation, the surplus pressure within the droplet amplifies with the increase in surface tension, as elaborated in Section VI B. This augmented pressure contributes to the increase in total maximum deformation as the droplet traverses the stenosed region, as evidenced in Fig. 23 (a). The expanded cross-sectional area significantly mitigates hydrodynamic resistance, resulting in a downfall in $R$ for surface tension ratios within $250 < \sigma^* \leq 375$, as observed in Fig. 22 (b). However, for $\sigma^* > 375$, hydrodynamic resistance increases with surface tension due to the increase in wall curvature effect at higher $\sigma^*$ values. This increased curvature opposes the flow, leading to a rise in channel hydrodynamic resistance. Conversely, in the non-stenosed channel, $R$ exhibits a slight increase with $\sigma^*$ (see Fig. 22 (b)). This suggests that the curvature effect is less pronounced in the non-stenosed channel, as the droplet does not make direct contact with the channel wall.

Fig. 22 (c) shows the effect of $\rho^*$ on hydrodynamic resistance in stenosed and non-stenosed channels. The hydrodynamic resistance exponentially increases with $\rho^*$. It is observed that the increasing rate of $R$ in stenosed channels is greater when $\rho^* \geq 1$, than that for $\rho^* < 1$. This can be attributed to more increase in pressure inside the droplet with the density when $\rho^* \geq 1$, as seen in Appendix F, Fig. 35.

The effect of $D^*$ on $R$ is shown in Fig. 22 (d). The hydrodynamic resistance increases with $D^*$ for both $D^* < 1$ and $D^* \geq 1$. However for $D^* < 1$, where the droplet does not have any contact with the stenosed region, the resistance is comparatively much less compared to the case of $D^* \geq 1$, as also observed during the droplet's entry process in Sec. VI A.2. Also, as $D^*$ increases wall deformation increases, and the same can be seen in Fig. 23 (b).

### D. Modified Ohnesorge number: a tool for predicting complete blockage mimicking stroke or heart attack

In this subsection, we conclude our discussion on the effect of various parameters ($\mu^*, \sigma^*, \rho^*, D^*$) by quantifying the prediction of blockages in confined microchannel. First, the dependency of lubrication film formation on $Oh^*$ and its influence on entry and passage times is examined. Subsequently, the blockage prediction using $Oh^*$ is presented, followed by a discussion on strategies for mitigating and eliminating blockages in the micorchannel.

The Ohnesorge number ($Oh$) [67] is a non-dimensional number, which can relate the forces acting on a droplet, expressed as:

$$\text{Ohnesorge number, } Oh = \frac{\mu_d}{(\sigma_d \rho_d D)^{0.5}} \tag{14}$$

Ohnesorge number, $Oh$ (Eq. 13) provides information about the relative importance of viscous and surface tension forces acting in a system. This number is also crucial in predicting the onset of different flow regimes, such as droplet formation, jet breakup, and coalescence [68,69]. As seen in Eq. 14, generally $Oh$ is defined only for one phase (either continuous or dispersed), while the phenomena of blockage are dependent on the properties of both continuous phase and the droplet, and for stenosed channel it will also depend on the degree of stenosis. Therefore, a modified Ohnesorge number ($Oh^*$) is proposed in this study, which has all these properties in the normalized form, as discussed in Sec. IV.

$$\text{Modified Ohnesorge number, } Oh^* = \frac{\mu^*}{(\sigma^* \rho^* D^*)^{0.5}} \tag{15}$$

As explained in Sec IV, the viscosity and the density of the droplet are normalised by the viscosity and the density of the continuous phase used in the study. The droplet's surface tension is normalized using the surface tension values of WBCs available in the literature [60], while the droplet diameter is normalized by the size of the stenosed cross section ($s$, see Fig. 1).

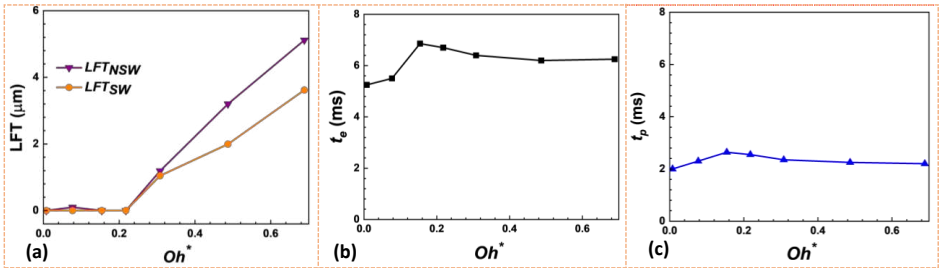


**Fig. 24.** Plot for variation in (a) lubrication film thickness ($LFT$), (b) entry time ($t_e$), and (c) passage time ($t_p$) with the increase in $Oh^*$ values.

Fig. 24 (a) shows the lubrication film thickness ($LFT$) in terms of $Oh^*$. It can be observed that the $LFT$ is close to zero at lower values of $Oh^*$ ($\leq 0.2015$) and so the resistance from the surrounding walls is higher. When $LFT$ is at marginal levels, it becomes evident that both $t_e$ and $t_p$ increase in with $Oh^*$, as shown in Fig. 24 (b) and Fig. 24 (c), respectively. However, as the lubrication film begins to develop for $Oh^*$ values exceeding 0.2, there is a noticeable decrease in both $t_e$ and $t_p$. As $Oh^*$ continues to increase, the $t_e$ and $t_p$ values stagnate, indicating a stabilization in the entry and passage time's response to the changing $Oh^*$ values. In other words, for $Oh^* \gg 0.2$, rate of increase in $t_e$ and $t_p$ becomes negligible.

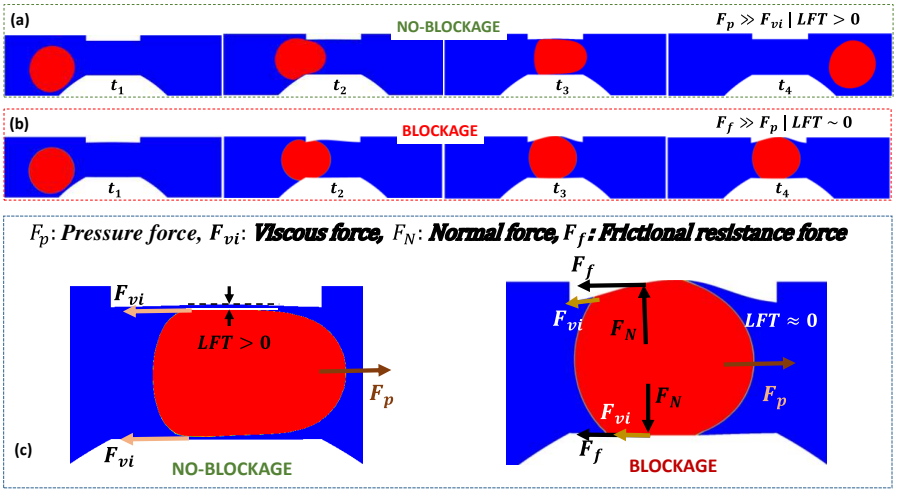


**Fig. 25.** The representative simulated image of phase contour showing (b) no-blockage and (b) blockage cases, and (c) the forces acting during no-blockage and blockage cases, respectively.

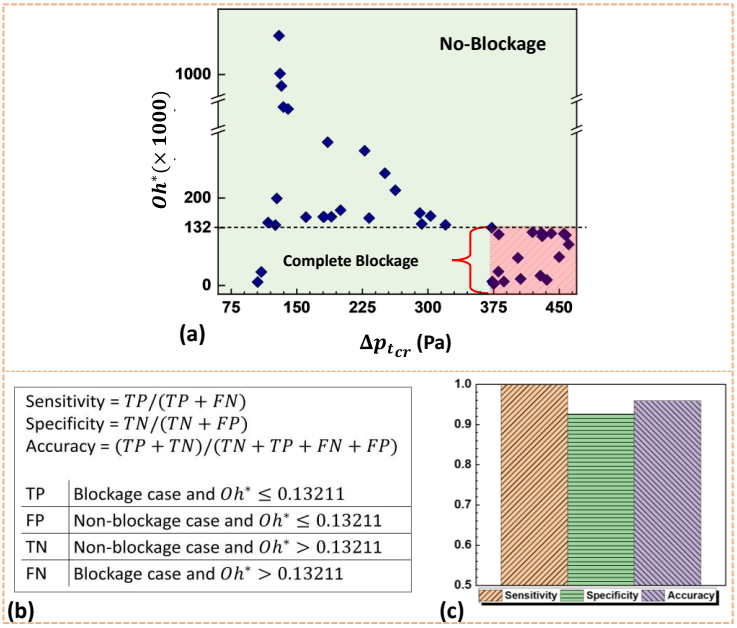


**Fig. 26.** Blockage prediction and sensitivity analysis. (a) Critical modified Ohnesorge number for the prediction of complete blockage of confined microchannels, (b) definitions of true positive ($TP$), true negative ($TN$), false

positive ($FP$) and false negative ($FN$) used for our sensitivity analysis, and (c) the sensitivity, specificity, and accuracy of blockage prediction.

A representative simulated image, each for a no-blockage and blockage case is shown in Fig. 25 (a) and (b), respectively. In no-blockage cases, the droplet passes through the stenosed region completely, while in blockage cases, the droplet gets stuck into the stenosed region. The forces acting during no-blockage and blockage cases are shown in Fig. 25 (c). The major forces consist of $F_p$ (pressure force), $F_{vi}$ (viscous force), $F_N$ (normal force), and $F_f$ (frictional resistance). $F_p$ represents the force due to the generated pressure different across the droplet while passing through the stenosed region. $F_{vi}$ represents the resistive force applied from the viscous lubrication film while passing through the stenosed region. $F_f$ represents the resistive force applied from the stenosed region wall due to the direct contact of the droplet with the stenosed channel wall. A no-blockage case can be characterized by two key attributes,

(i) $LFT > 0$: The positive value of $LFT$ suggests that the droplet can move through the stenosed region, indicating that there is no complete obstruction.
(ii) $F_p \gg F_{vi}$: The $F_p$ significantly surpasses $F_{vi}$, signifying that the primary driving force for droplet movement is the pressure differential, and the viscous force of the fluid has a relatively minor effect. This is often the case when the channel is not severely constricted.

In contrast, a blockage case is represented by the following characteristics:
(i) $LFT \approx 0$: Here, the value of $LFT$ is close to zero, suggesting that the droplet encounters a significant obstacle from the channel wall, preventing it from freely passing through.
(ii) $F_f \gg F_p$: The frictional resistance becomes the dominant force in this scenario, outweighing the pressure force. This indicates that the droplet becomes stuck or immobilized within the stenosed region due to the strong influence of friction, which prevents it from moving further.

In Figure 26 (a), the forecast of complete blockage is depicted in relation to the modified Ohnesorge number. Here, $Oh^*$ is plotted against $\Delta p_{t_{cr}}$, representing the maximum pressure drop across the stenosed section, as explained in Sec. V B. When $Oh^*$ is greater than $0.132$, the stenosed channel maintains droplet transport. Conversely, if $Oh^* \leq 0.132$, the channel undergoes a complete blockage, ceasing the droplet movement entirely. Analogously, envisioning this scenario as a narrowed blood vessel with droplets symbolizing cells, the cessation of blood cell supply through the artery could lead to severe health complications like stroke and heart attack. Additionally, the proposed number demonstrates that for non-stenosed channels (having $D^* < 1$), i.e., large $Oh^*$, blockages won't occur. The significance of $Oh^*$ illustrated in Fig. 26 (a) lies in its capacity to anticipate blockage scenarios in blood vessels across diverse parameter values, encompassing viscosity, surface tension, density, droplet diameter, and stenosis degree, using a single dimensionless number.

Sensitivity analysis is a method to evaluate the accuracy of the microfluidic device by measuring how well it can predict the blockage in different scenarios. It is based on the definitions of true positive, true negative, false positive, and false negative droplets, which depend on the values of the modified Ohnesorge number ($Oh^*$). Sensitivity analysis can calculate the sensitivity, specificity, and accuracy of the predicting tool for each value of $Oh^*$. These metrics indicate how effective the device is in predicting blockage or non-blockage cases. Fig. 26 (b) briefly shows the definitions of sensitivity, specificity, and accuracy along with the definitions of true positive (TP), false positive (FP), true negative (TN), and false negative (FN) corresponding to the values of $Oh^*$. An elaborative explanation of the former three terms is given below:

(a) Sensitivity: This is the ability of a prediction tool to correctly identify the condition with blockage. It is the proportion of cases with $Oh^* \leq 0.132$ and have shown blockage or in other words have a positive test, or the true positive rate. It can be calculated using the equation: sensitivity = number of true positives / (number of true positives + number of false negatives) or $TP/(TP + FN)$.

(b) Specificity: This is the ability of a prediction tool to correctly identify the condition without the blockage. It is the proportion of cases with $Oh^* \geq 0.132$ and have shown non-blockage or in other words have a negative test, or true negative rate. It can be calculated using the equation: specificity = number of true negatives / (number of true negatives + number of false positives) or $TN/(TN + FP)$.

(c) Accuracy: This is the percentage of correct predictions made by the model. A prediction tool is said to be accurate when it measures what it is supposed to measure. In the present study, blockage cases for $Oh^* \leq 0.132$ and non-blockage cases for $Oh^* \geq 0.132$, are the desired output from the proposed prediction model. It can be calculated using the equation: accuracy = (number of true positives + number of true negatives) / (number of true negatives + number of true positives + number of false positives + number of false negatives) or $(TP + TN)/(TN + TP + +FP + FN)$.

Fig. 26 (c) depicts the calculated sensitivity, specificity, and accuracy of the proposed prediction model. The prediction of the blockage based on the modified Ohnesorge has a sensitivity of 1, specificity of 0.926, and accuracy of 0.959.

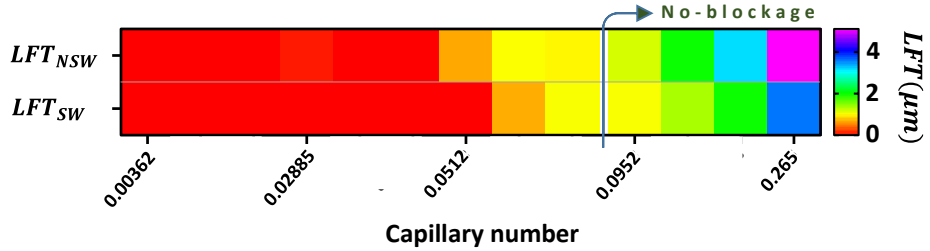


**Fig. 27.** Regime of no-blockage cases in terms of Capillary number ($Ca_{max}$).

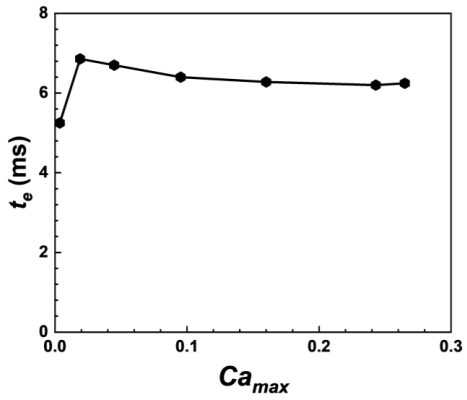


**Fig. 28.** Variation in the droplet entry time ($t_e$) in terms of Capillary number ($Ca_{max}$).

It is observed that the increasing Capillary number increases the $LFT$, [2] both in the vicinity of the stenosed and the non-stenosed wall, as shown in Fig. 27. Further, it can be observed that the film thickness is higher in the vicinity of the non-stenosed wall than that in the stenosed wall. Due to the existence of the thicker lubrication layer, the droplet movement through the stenosed region smoothens, which facilitates the easy passage of the droplet through the stenosed channel at higher Capillary numbers ($\geq 0.095$). The throttling of the entry time at higher values of Capillary numbers can be seen in Fig. 28. Therefore, it can be concluded that the blockage cases are not observed at higher Capillary numbers. So, to avoid blockage for a given droplet-continuous properties, the flow velocity should be increased such that the Capillary number lies in the range of no blockage zone.

**E. Effect of channel stiffness on the droplet motion into the deformable stenosed region**

The wall stiffness also plays a role in the entry and passage process of the droplet. In the Sec. VI B, $LFT$ was observed to be more in the vicinity of the non-stenosed wall as compared to the stenosed wall, where the stenosed wall was comparatively more rigid than the non-stenosed wall. In this subsection, the role of channel stiffness ($0.1 \leq Y^* \leq 2$), i.e., $8.1486 \times 10^{-6} \leq f_p \leq 4.0743 \times 10^{-7}$ on the droplet motion is investigated. Similar to the observation presented in Sec. VI B, the $LFT$ is less in the vicinity of the stenosed wall (comparatively rigid) than that in the non-stenosed wall, as shown in Fig. 29 (a). Further, Fig. 29 (a) shows that the $LFT$ goes on decreasing with the increase in wall stiffness. The effect of this is reflected in the increasing $t_e$ with the wall stiffness, as shown in Fig. 29 (b). However, the effect of stiffness on $t_p$ is different because of the dominating wall curvature effect at lower stiffness values, as shown in Fig. 29 (c). As $Y^*$ decreases, wall deformation increases. This brings in the curvature effect at the droplet-wall interface. The wall curvature results into higher normal force applied from the wall to the droplet (shown in Fig. 25(c)) and thus higher friction resistance force $(F_f)$, which hinders the droplet motion through the stenosed region. Therefore, $t_p$ is maximum for the least stiff wall. Fig. 29 (d) shows the hydrodynamic resistance of the channel ($R$) with respect to the rigid channel ($R_{rigid}$). The hydrodynamic resistance increases with the increase in wall stiffness due to a decrease in wall compliance. However, it should be noted here that the hydrodynamic resistance of the channel for the droplet passage process with least $Y^*$ is $\sim$95%, which is only 5% decrement in the hydrodynamic resistance compared to rigid stenosed channels. This demonstrates that wall compliance does not have a significant effect on the hydrodynamics resistance for the passage process. This can be attributed to the dominating wall curvature effect at lower $Y^*$. This finding is in contrast with the hydrodynamic resistance of single-phase flow through compliance microchannels, where significant decrement in the resistance is observed for single-phase flow [49,70]. The curvature effect leading to a higher passage time of droplet through deformable stenosed channels indicate that the chance of blockage/stroke is higher for a deformable stenosed channel or the blood vessel in case of cardiovascular diseases like stroke. This finding is in line with a previous clinical study, which states occurrence of stroke is more frequent in patients with deformable stenosed vessels [71].

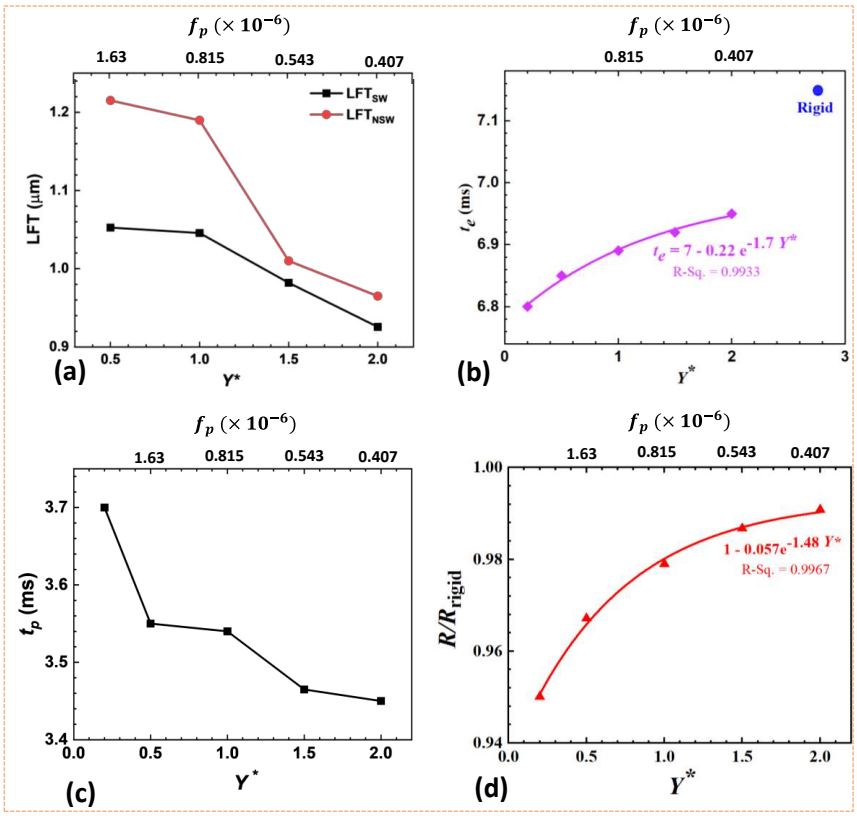


**Fig. 29.** Effect of wall stiffness on (a) lubrication film thickness ($LFT$), (b) entry time ($t_e$), (a) paasage time ($t_p$), and (d) hydrodynamic resistance with respect to rigid channel ($R/R_{rigid}$).

## VII. CONCLUSIONS

This study showcased the ability to model the droplet migration through a deformable section of a stenosed and non-stenosed microchannel. A two-way FSI model was used to couple the transient behavior of the droplet and the deformable channel wall.

This work has explored the interplay between various physical properties that impact the movement of droplets through confined microchannel, and ultimately lead to blockage. The study has focused on understanding the flow dynamics in narrowed microchannels to identify a critical modified Ohnesorge number that can serve as an indicator for the occurrence of complete blockage in the channel.

Following are some of the major highlights and insights from the present study:

1. The properties of both droplets and continuous phase are very crucial in predicting blockages in a microchannel.
2. Among the physical properties (i.e., viscosity, surface tension, and density), surface tension has a dominating role in building pressure both in the channel and inside the droplet, wall deformation, and hydrodynamic resistance.
3. At higher viscosities ($\mu^* > 2$), a lubrication film develops between the droplet and the channel wall, facilitating the smooth entry of the droplet, despite experiencing a high viscous resistance. With the increase in $\mu^*$, the core of eddies starts shifting away from the walls of the stenosed region.
4. The entry time has linear dependency on the diameter ratio, with the slope being ~80°.
5. The effect of droplet density on entry and passage processes is studied. Droplets with higher density carry higher momentum at the same velocity. Thus, the inertial effect dominates during the entry process, which allows a faster entry for droplets with higher density. Whereas pressure inside the droplet increases during passage for droplets with higher density, which increases the contact with the wall and hence the resistive force applied onto the droplet. This results in almost comparable passage time for droplets of distinct densities.
6. The effect of $\sigma^*$ on the wall deformation is more significant as compared to $\mu^*$. This can be attributed to the higher droplet's internal Laplace pressure arising due to surface tension compared to the viscosity-induced pressure.
7. At higher surface tension values, the curvature effect in the deformable wall becomes significant and opposes the droplet movement, significantly slowing down the entry and passage processes. Thus, despite the increased cross-sectional area of the channel at higher surface tension, hydrodynamic resistance increases due to the curvature effect.
8. For a 37% degree of stenosis, around 417% increment in hydrodynamics resistance ($R$) is observed with respect to the non-stenosed channel at $\mu^* = 4$.
9. The increasing rate of $R$ in the stenosed channel is greater when $\rho^* \geq 1$, than that for $\rho^* < 1$. This can be attributed to a higher increase in pressure inside the droplet with the density when $\rho^* \geq 1$.
10. A modified *Ohnesorge number* $\left(Oh^* = \frac{\mu^*}{(\sigma^*\rho^*D^*)^{0.5}}\right)$ is proposed to predict the chances of complete blockage in a deformable stenosed microchannel. The lubrication film thickness, entry time, and passage time, all show dependency on the $(Oh^*)$. $LFT$ is marginal for $Oh^* \leq 0.2015$, evolving into a favorable factor for the occurrence of blockage.
11. A critical value for modified Ohnesorge number ($Oh^* \leq 0.132$) is found below which the probability of the occurrence of the complete blockage is very high. The increased Laplace pressure and the increased curvature effect because of the increase in wall deformation were the main factors behind ceasing the droplet movement into the stenosed channel.
12. The blockage prediction model based on the modified Ohnesorge is found to have a sensitivity of 100%, specificity of 92.6%, and accuracy of 95.9%.
13. The formation of lubrication film has shown dependence on Capillary number too. A lubrication film always exists between the droplet and the wall for $Ca_{max} \geq 0.095$, and $LFT$ increases with an increase in Capillary number. The film thickness is more pronounced in the vicinity of the non-stenosed wall than in the stenosed wall. The lubrication film facilitates smooth entry and passage of the droplet through the stenosed channel,

so its existence helps prevent complete blockage and can thus prevent fatal diseases arising due to channel (blood vessel) blockage. With the increase in flow velocity, $Ca_{max}$ will also increase, leading to an increase in $LFT$ and thus attenuating the chances of blockage.

14. The effect of channel wall stiffness is also investigated. While the lower stiffness is favourable for the droplet's entry but not for the droplet's passage. When the wall stiffness is lower, a higher $LFT$ is observed, resulting in a shorter $t_e$. However, for the passage process, the curvature effect is dominant at lower $Y^*$, causing an increase in $t_p$ for lower stiffness. This concludes that, though the entry process is favoured by the wall deformability, the chances of droplet blockage during the passage process are higher for a deformable stenosed channel.

The current study explores the dynamics of droplet motion through narrowed microchannels, offering insights applicable to addressing modern challenges in microfluidics, particularly in cardiovascular health. The insights gained offer a pathway for understanding cell migration through constricted blood vessels, crucial for tackling issues like stroke and heart attack development. By examining how parameters such as the modified Ohnesorge Number and Capillary Number affect droplet (mimicking cell behaviour) migration, the extension of this study can help in developing a novel approach for assessing cardiovascular risk and preventing blockages in stenosed blood vessels.

However, it's essential to acknowledge certain limitations that may be explored in the future. The limitations of the present study may arise from the simplified droplet and channel models. Studying a single droplet in the specific constricted microchannel configuration may not adequately represent real-world complexities where multiple droplets interact or where channel geometry varies non-linearly. Moreover, scaling issues challenge the direct application of results to larger systems. In context to biomedical applications, Newtonian droplets and simplified stenosed channel may not accurately represent real cell complexity and vessel conditions. In vitro approaches may not fully reflect in vivo complexities, and may limit direct disease prediction.

## ACKNOWLEDGEMENTS

The author A.R. would like to thank the Science and Engineering Research Board (SERB), Department of Science and Technology (DST), Government of India for the financial support under Grant No. SRG/2020/002268. The author A.A. would like to thank the Department of Science and Technology, Government of India, for the financial support under Grant No. DST/INSPIRE/04/2019/001001. Also, we would like to acknowledge the CAD lab of IIT Patna for providing essential workstation facilities for our simulation work. Additionally, we are grateful to Dr. Manoj Kumar Tripathi (Assistant Professor, Chemical Engineering, Indian Institute of Science Education and Research Bhopal, Madhya Pradesh, India) for his valuable directions for drawing streamlines within the droplet.

## NOMENCLATURE

| *Symbols* | | |
|---|---|---|
| $H$ | Total height of the channel | [$\mu$m] |
| $W$ | Width of the domain | [$\mu$m] |
| $L$ | Total length of the domain | [$\mu$m] |
| $Q$ | Flow rate | [$\mu l$-m$^{-1}$] |
| $t$ | Thickness of the stenosed portion | [$\mu$m] |

| | | |
|---|---|---|
| $l_e$ | Length of the droplet along flow direction | [$\mu$m] |
| $t_{cr}$ | Time at which pressure across the stenosed region is maximum | [ms] |
| $h$ | Top wall thickness | [$\mu$m] |
| $s$ | Undeformed height between stenosed wall and the top wall | [$\mu$m] |
| $Y$ | Young's Modulus | [MPa] |
| $\mu$ | Viscosity | [N-s/m$^2$] |
| $\rho$ | Density | [kg/m$^3$] |
| $\sigma$ | Surface tension | [N/m] |
| $\overrightarrow{S_t}$ | Source term representing force due to surface tension | [N] |
| $\theta_A$ | Advancing contact angle | [Degree] |
| $F$ | Force | [N] |
| $\Delta p$ | Pressure drop | [Pa] |
| $R$ | Hydrodynamic resistance | [N-s/m$^5$] |

*Dimensionless parameters*

| | |
|---|---|
| $Re$ | Reynolds number |
| $Ca_{max}$ | Capillary number ($\mu_d u_{in}/\sigma$) |
| $\mu^*$ | Viscosity ratio ($\mu_d/\mu_c$) |
| $\rho^*$ | Density ratio ($\rho_d/\rho_c$) |
| $\sigma^*$ | Surface tension ratio ($\sigma_d/\sigma_w$) |
| $D^*$ | Normalised diameter ($D/s$) |
| $\lambda$ | Elongation ratio ($l_e/D$) |
| $Oh$ | Ohnesorge number $\mu_d/\sqrt{(\sigma_d \rho_d D)}$ |
| $Oh^*$ | Modified Ohnesorge number $\mu_d^*/\sqrt{(\sigma_d^* \rho_d^* D^*)}$ |

*Subscripts*

| | |
|---|---|
| $a$ | artery |
| $c$ | Continuous phase |
| $d$ | Dispersed phase |
| $w$ | White blood cell |
| $A$ | Advancing contact angle |
| $f$ | Frictional resistance |
| $vi$ | Viscous (force) |
| $N$ | Normal (force) |

*Abbreviations*

| | | |
|---|---|---|
| *WSS* | Wall shear stress | [Pa] |

**APPENDIX A: Streamlines behaviour during droplet entry at different $\mu^*$**

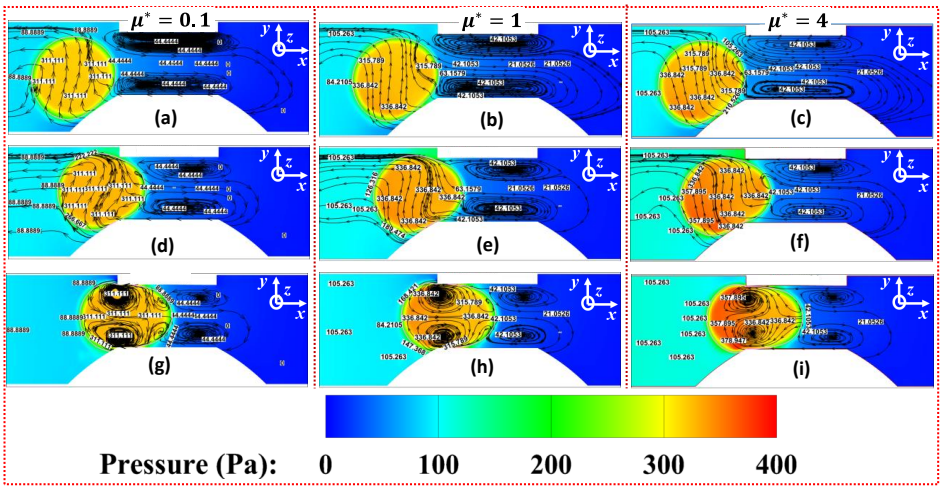


**Fig. 30.** Pressure contours ($xy$ plane) along with the streamlines (in the relative reference frame which moves with the droplet) for different viscosity ratios during entry process. The three different positions of the droplet during the entry is shown, respectively, for $\mu* = 0.1$, 1, and 4.

Fig. 30 depicts the flow adjustments inside the droplet during its entry into the stenosed region. The streamlines shown here are drawn in relative reference frames that keep changing with the droplet movement. It can be observed that for every $\mu^*$values, the two eddies are always present downstream of the droplet throughout the droplet motion into the stenosed region. Also, the extension (length) of the streamlines along the flow direction keeps decreasing with the droplet motion into the stenosed region. Further, no eddies appear inside the droplet till the droplet enters more than half into the stenosed region. Two eddies develop near the contact point of the droplet and the walls (see Fig. 30 g-i). This indicates the adjustment of the flow within the droplet in response to the hindrance to the flow and thus becomes a factor in increasing the droplet's internal pressure. Two crucial takeaways from the streamlines inside the droplet can be considered; firstly, the core of the eddies formed inside the droplet are more closer to the stenosed region in case of $\mu^* = 0.1$, and it gradually goes away from the channel walls with the increase in $\mu^*$. Secondly, the density of the eddies inside the droplet keeps decreasing with the increase in $\mu^*$. Four eddies can be seen inside the droplet for $\mu^* = 0.1$ (see Fig. 30 g; two near the wall and two near the leading edge of the droplet), and two eddies inside the droplet for $\mu^* = 1$ and 4 (see Fig. 30 h-i). These two phenomena can be attributed to the evolvement of the lubrication layer between the droplet and the wall with the increase in $\mu^*$. The presence of the core away from the stenosed wall actually helps in the droplet's smoother entry.

**APPENDIX B: Streamlines behaviour during droplet entry at different $\sigma^*$**

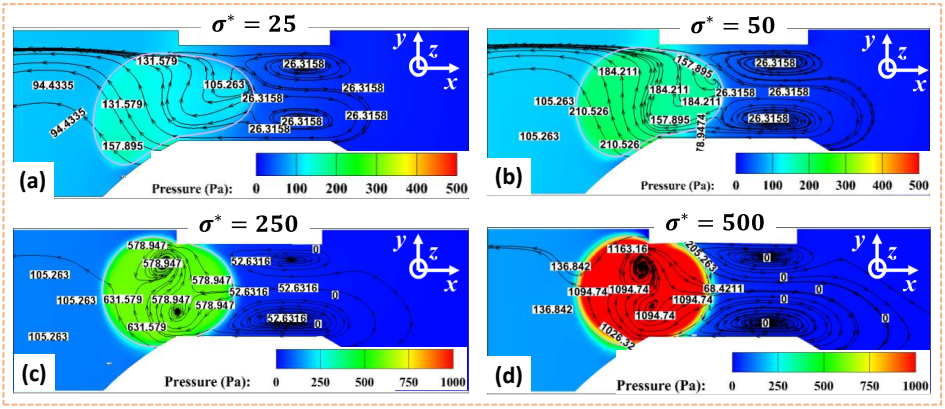


**Fig. 31.** Pressure contours (*xy*-plane) along with the streamlines (in the relative reference frame which moves with the droplet) for different surface tension ratios during entry process: (a) $\sigma^* = 25$, (b) $\sigma^* = 50$, (c) $\sigma^* = 250$, and (d) $\sigma^* = 500$. The legends for pressure for $\sigma^* = 250$ and 500 are different than that of $\sigma^* = 25$ and 50, for the sake of proper quantitative representation.

Figure 31 depicts pressure contours (xy-plane) and streamlines (in the relative reference frame moving with the droplet) at various surface tension ratios during droplet's entry. At lower values of $\sigma^*$, when the droplet has no contact with the walls, no eddies develop inside the droplet. However, at higher values of $\sigma^*$, when the droplet comes in contact with a stenosed region, two eddies can be observed inside the droplet near the point of contact.

## APPENDIX C: Effect of viscosity on the velocity profile

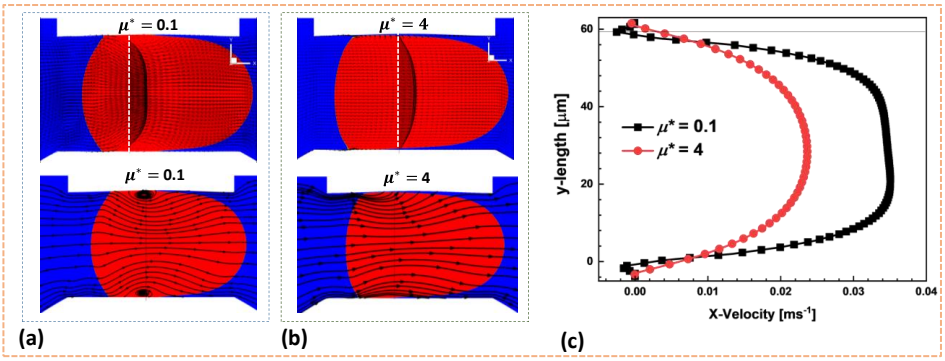


**Fig. 32** Velocity profile and streamlines for (a) $\mu^* = 0.1$ and (b) $\mu^* = 4$, and (c) velocity plot along the dotted lines shown in top figures of (a) and (b).

At lower viscosity ratios, significant droplet-wall contact occurs, leading to the formation of recirculation zones, as shown in Fig. 32 (a), which is unlike the case at higher $\mu^*$ (see Fig. 32 (b)). This phenomenon results in reverse velocity near the walls of the stenosed region, as illustrated in Fig. 32 (c).

**APPENDIX D: Streamlines behaviour during droplet passage at different $\mu^*$**

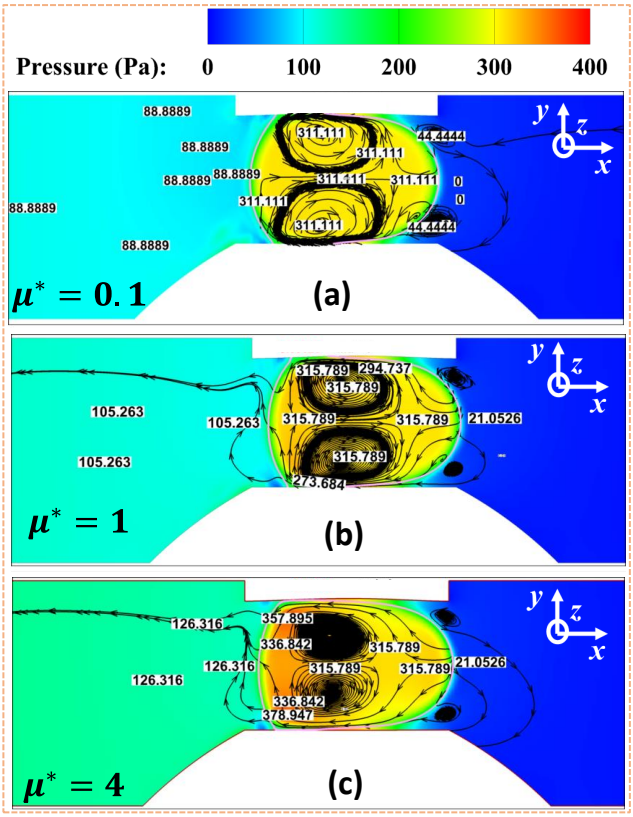


**Fig. 33.** Pressure contours (*xy*-plane) along with the streamlines (in the relative reference frame which moves with the droplet) for different viscosity ratios during passage process: (a) $\mu^* = 0.1$, (b) $\mu^* = 1$, and (c) $\mu^* = 4$.

As observed during the entry process, the core of the two eddies moves further away from the walls as the viscosity ratio increases. This same pattern continues during the passage process, as shown in Fig. 33. Notably, it is evident that the core of the eddies is positioned farthest from the walls during the passage process in the following order: highest in $\mu^* = 4$, followed by $\mu^* = 1$ , and then $\mu^* = 0.1$. This indicate a smoother passage at higher $\mu^*$.

## APPENDIX E: Streamlines behaviour during droplet passage at different $\sigma^*$

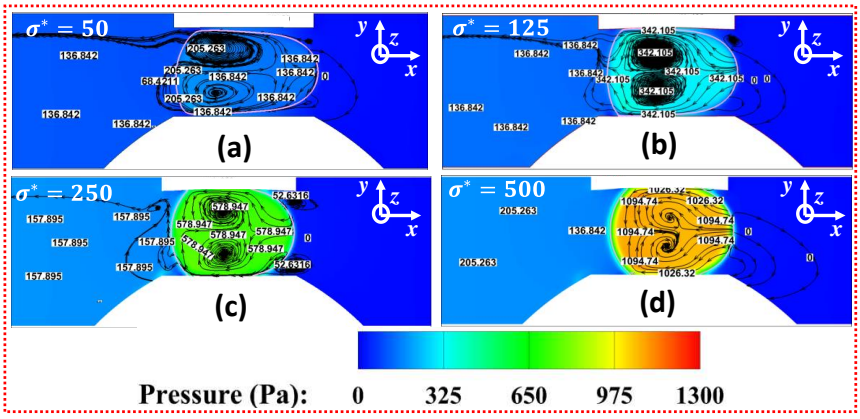


**Fig. 34.** Pressure contours along ($xy$-plane) with the streamlines (in the relative reference frame which moves with the droplet) for different surface tension ratios during passage process: (a) $\sigma^* = 25$, (b) $\sigma^* = 125$, (c) $\sigma^* = 250$, and (d) $\sigma^* = 500$.

## APPENDIX F: Effect of density on the passage process

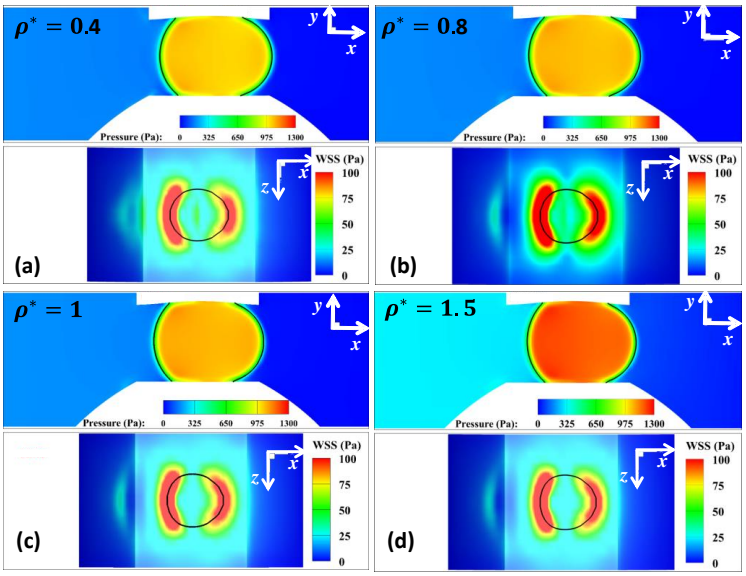


**Fig. 35.** Contours for pressure along the flow direction ($xy$-plane) and the $WSS$ at the same instant on the top surface ($xz$-plane) of the stenosed wall for (a) $\rho^* = 0.4$, (b) $\rho^* = 0.8$, (c)$\rho^* = 1$, and (d) $\rho^* = 1.5$.

## APPENDIX G: Effect of diameter on the passage process

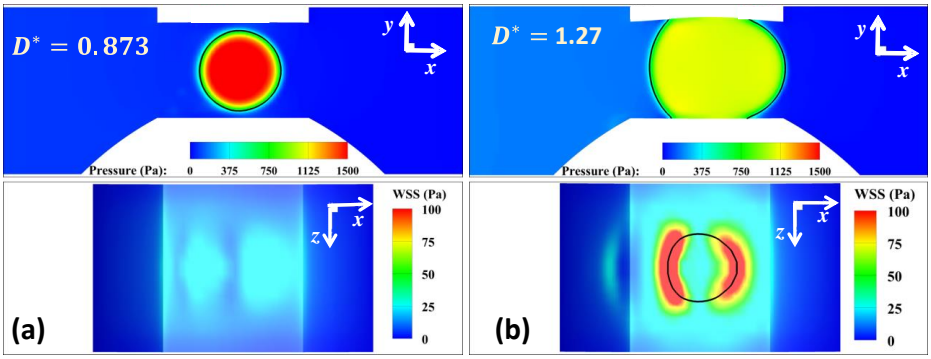


**Fig. 36.** Contours for pressure along the flow direction ($xy$-plane) and the $WSS$ at the same instant on the top surface ($xz$-plane) of the stenosed wall for (a) $D^* = 0.873$, and (b) $D^* = 1.27$.

## DATA AVAILABILITY

The data that support the findings of this study is available from the corresponding author upon request.

## CONFLICT OF INTEREST

The authors have no conflict of interest.

## REFERENCES

[1] Z. Jiao, L. Zhao, C. Tang, H. Shi, F. Wang, and B. Hu, *Droplet-Based PCR in a 3D-Printed Microfluidic Chip for MiRNA-21 Detection*, Anal. Methods **11**, 3386 (2019).

[2] A. Singla and B. Ray, *Effects of Surface Topography on Low Reynolds Number Droplet/Bubble Flow through a Constricted Passage*, Phys. Fluids **33**, (2021).

[3] R. Seemann, M. Brinkmann, T. Pfohl, and S. Herminghaus, *Droplet Based Microfluidics*, Reports Prog. Phys. **75**, 16601 (2011).

[4] H. Feng, T. Zheng, M. Li, J. Wu, H. Ji, J. Zhang, W. Zhao, and J. Guo, *Droplet-Based Microfluidics Systems in Biomedical Applications*, Electrophoresis **40**, 1580 (2019).

[5] L. Shang, Y. Cheng, and Y. Zhao, *Emerging Droplet Microfluidics*, Chem. Rev. **117**, 7964 (2017).

[6] E. Kjeang, N. Djilali, and D. Sinton, *Microfluidic Fuel Cells: A Review*, J. Power Sources **186**, 353 (2009).

[7] C.-M. Ho and Y.-C. Tai, *Micro-Electro-Mechanical-Systems (MEMS) and Fluid Flows*, Annu. Rev. Fluid Mech. **30**, 579 (1998).

[8] W. L. Olbricht, *Pore-Scale Prototypes of Multiphase Flow in Porous Media*, Annu. Rev. Fluid Mech. **28**, 187 (1996).

[9] C. Richard, A. Neild, and V. J. Cadarso, *The Emerging Role of Microfluidics in Multi-Material 3D Bioprinting*, Lab Chip **20**, 2044 (2020).

[10] S. H. Au et al., *Clusters of Circulating Tumor Cells Traverse Capillary-Sized Vessels*, Proc. Natl. Acad. Sci. U. S. A. **113**, 4947 (2016).

[11] Z. Zhang, J. Xu, B. Hong, and X. Chen, *The Effects of 3D Channel Geometry on CTC Passing Pressure-towards Deformability-Based Cancer Cell Separation*, Lab Chip **14**, 2576 (2014).

[12] R. M. Hochmuth, *Micropipette Aspiration of Living Cells*, J. Biomech. **33**, 15 (2000).

[13] J. Ren, Y. Liu, W. Huang, and R. H. W. Lam, *A Narrow Straight Microchannel Array for Analysis of Transiting Speed of Floating Cancer Cells*, Micromachines **13**, 1 (2022).

[14] F. Y. Leong, Q. Li, C. T. Lim, and K. H. Chiam, *Modeling Cell Entry into a Micro-Channel*, Biomech. Model. Mechanobiol. **10**, 755 (2011).

[15] Z. S. Khan, N. Kamyabi, F. Hussain, and S. A. Vanapalli, *Passage Times and Friction Due to Flow of Confined Cancer Cells, Drops, and Deformable Particles in a Microfluidic Channel*, Converg. Sci. Phys. Oncol. **3**, 024001 (2017).

[16] J. Ma, Q. Huang, Y. Zhu, Y. Q. Xu, and F. B. Tian, *Effects of Fluid Rheology on Dynamics of a Capsule through a Microchannel Constriction*, Phys. Fluids **35**, (2023).

[17] X. Zhang, X. Chen, and H. Tan, *On the Thin-Film-Dominated Passing Pressure of Cancer Cell Squeezing through a Microfluidic CTC Chip*, Microfluid. Nanofluidics **21**, 1 (2017).

[18] M. I. H. Khan, M. U. H. Joardder, C. Kumar, and M. A. Karim, *Multiphase Porous Media Modelling: A Novel Approach to Predicting Food Processing Performance*, Crit. Rev. Food Sci. Nutr. **58**, 528 (2018).

[19] Z. Zhang, J. Xu, and C. Drapaca, *Particle Squeezing in Narrow Confinements*, Microfluid. Nanofluidics **22**, 1 (2018).

[20] Z. Wang, R. Lu, W. Wang, F. B. Tian, J. J. Feng, and Y. Sui, *A Computational Model for the Transit of a Cancer Cell through a Constricted Microchannel*, Biomech. Model. Mechanobiol. 1129 (2023).

[21] Z. Tang, F. Yaya, E. Sun, L. Shah, J. Xu, A. Viallat, E. Helfer, and Z. Peng, *Analytical Theory for a Droplet Squeezing through a Circular Pore in Creeping Flows under Constant Pressures*, Phys. Fluids **35**, (2023).

[22] D. Shayunusov, D. Eskin, H. Zeng, and P. A. Nikrityuk, *Behavior of Small Water Droplets in a Highly Viscous Flow in a Converging and Diverging Channel*, Phys. Fluids **36**, 33333 (2024).

[23] G. Roure, A. Z. Zinchenko, and R. H. Davis, *Numerical Simulation of Deformable Droplets in Three-Dimensional, Complex-Shaped Microchannels*, Phys. Fluids **35**, (2023).

[24] Z. Zhang, C. Drapaca, X. Chen, and J. Xu, *Droplet Squeezing through a Narrow Constriction: Minimum Impulse and Critical Velocity*, Phys. Fluids **29**, (2017).

[25] M. A. Hashem, A. Aghilinejad, X. Chen, and H. Tan, *Compound Droplet Modeling for Circulating Tumor Cell Microfiltration with Adaptive Meshing Refinement*, J. Fluids Eng. Trans. ASME **142**, 1 (2020).

[26] E. Kadivar, *Modeling Droplet Deformation through Converging–Diverging Microchannels at Low Reynolds Number*, Acta Mech. **229**, 4239 (2018).

[27] Z. Zhang, C. Drapaca, D. Gritsenko, and J. Xu, *Pressure of a Viscous Droplet Squeezing through a Short Circular Constriction: An Analytical Model*, Phys. Fluids **30**, (2018).

[28] A. K. Nema, M. K. Tripathi, and K. C. Sahu, *Migration of a Viscoelastic Drop in a Ratchet Microchannel*, J. Nonnewton. Fluid Mech. **307**, 104870 (2022).

[29] I. V. Kravchenko, S. A. Patlazhan, and V. G. Sultanov, *Microfibers Formation in Two-Phase Fluid Flowing in a Channel with the Abrupt Constriction: Numerical Modeling*, J. Phys. Conf. Ser. **1556**, (2020).

[30] X. Zheng, J. Lu, B. Bai, and G. Tryggvason, *The Passage of a Bubble or a Drop Past an Obstruction in a Channel*, Phys. Fluids **32**, (2020).

[31] A. Raj, M. Dixit, M. Doble, and A. K. Sen, *A Combined Experimental and Theoretical Approach towards Mechanophenotyping of Biological Cells Using a Constricted Microchannel*, Lab Chip **17**, 3704 (2017).

[32] A. Raj, R. Halder, P. Sajeesh, and A. K. Sen, *Droplet Generation in a Microchannel with a Controllable Deformable Wall*, Microfluid. Nanofluidics **20**, 1 (2016).

[33] A. Raj and A. K. Sen, *Entry and Passage Behavior of Biological Cells in a Constricted Compliant Microchannel*, RSC Adv. **8**, 20884 (2018).

[34] A. Huerre, O. Theodoly, A. M. Leshansky, M. P. Valignat, I. Cantat, and M. C. Jullien, *Droplets in Microchannels: Dynamical Properties of the Lubrication Film*, Phys. Rev. Lett. **115**, 3 (2015).

[35] N. Freidoonimehr, R. Chin, A. Zander, and M. Arjomandi, *Effect of Shape of the Stenosis on the Hemodynamics of a Stenosed Coronary Artery*, Phys. Fluids **33**, (2021).

[36] X. Zhang, L. Zheng, M. Luo, C. Shu, and E. Wang, *Evaluation of Particle Shape, Size and Magnetic Field Intensity for Targeted Delivery Efficiency and Plaque Injury in Treating Atherosclerosis*, Powder Technol. **366**, 63 (2020).

[37] P. Eshtehardi, A. J. Brown, A. Bhargava, C. Costopoulos, O. Y. Hung, M. T. Corban, H. Hosseini, B. D. Gogas, D. P. Giddens, and H. Samady, *High Wall Shear Stress and High-Risk Plaque: An Emerging Concept HHS Public Access*, Int J Cardiovasc Imaging **33**, 1089 (2017).

[38] S. Pabi, M. Khan, S. K. Jain, A. K. Sen, A. Raj, and others, *Effect of Stenotic Shapes and Arterial Wall Elasticity on the Hemodynamics*, Phys. Fluids **35**, (2023).

[39] X. Zhang, M. A. Hashem, X. Chen, and H. Tan, *On Passing a Non-Newtonian Circulating Tumor Cell (CTC) through a Deformation-Based Microfluidic Chip*, Theor. Comput. Fluid Dyn. **32**, 753 (2018).

[40] T. Wu and J. J. Feng, *Simulation of Malaria-Infected Red Blood Cells in Microfluidic Channels: Passage and Blockage*, Biomicrofluidics **7**, (2013).

[41] K. Vahidkhah, P. Balogh, and P. Bagchi, *Flow of Red Blood Cells in Stenosed Microvessels*, Sci. Rep. **6**, 1 (2016).

[42] Z. Zhang, J. Xu, and X. Chen, *Compound Droplet Modelling of Circulating Tumor Cell Microfiltration*, in *ASME International Mechanical Engineering Congress and Exposition*, Vol. 57472 (2015), p. V07BT09A008.

[43] Z. Y. Luo, L. He, and B. F. Bai, *Deformation of Spherical Compound Capsules in Simple Shear Flow*, J. Fluid Mech. **775**, 77 (2015).

[44] E. Benet and F. J. Vernerey, *Mechanics and Stability of Vesicles and Droplets in Confined Spaces*, Phys. Rev. E **94**, 1 (2016).

[45] P. Poredoš and B. Žižek, *Plasma Viscosity Increase with Progression of Peripheral Arterial Atherosclerotic Disease*, Http://Dx.Doi.Org/10.1177/000331979604700306 **47**, 253 (1996).

[46] G. Késmárky, P. Kenyeres, M. Rábai, and K. Tóth, *Plasma Viscosity: A Forgotten Variable*, Clin. Hemorheol. Microcirc. **39**, 243 (2008).

[47] I. Miranda, A. Souza, P. Sousa, J. Ribeiro, E. M. S. Castanheira, R. Lima, and G. Minas, *Properties and Applications of PDMS for Biomedical Engineering: A Review*, J. Funct. Biomater. 2022, Vol. 13, Page 2 **13**, 2 (2021).

[48] D. Fuard, T. Tzvetkova-Chevolleau, S. Decossas, P. Tracqui, and P. Schiavone, *Optimization of Poly-Di-Methyl-Siloxane (PDMS) Substrates for Studying Cellular Adhesion and Motility*, Microelectron. Eng. **85**, 1289 (2008).

[49] A. Raj and A. K. Sen, *Flow-Induced Deformation of Compliant Microchannels and Its Effect on Pressure–Flow Characteristics*, Microfluid. Nanofluidics **20**, 1 (2016).

[50] N. D. Kankane and N. S. Bodke, *The Study of Flow Rate , Resistive Impedance of Blood Flowing through Stenosed Artery*, **6**, 30 (2017).

[51] ANSYS, *ANSYS System Coupling User's Guide; ANSYS® Academic Research, Release 19.1*.

[52] C. W. HIRT AND B. D. NICHOLS, *Hirt and Nichols - 1981 - Volume of Fluid (VOF) Method for the Dynamics of f(1).Pdf*, J. Comput. Phys. **39**, 201 (1981).

[53] Fluent Thoery Guide, *Ansys Fluent Theory Guide 2021-R1*, ANSYS Inc., USA **15317**, 724 (2021).

[54] T. C. Shidhore and I. C. Christov, *Static Response of Deformable Microchannels: A Comparative Modelling Study*, J. Phys. Condens. Matter **30**, (2018).

[55] J. D. Anderson and J. Wendt, *Computational Fluid Dynamics*, Vol. 206 (Springer, 1995).

[56] E. Wang and T. Nelson, *Structural Dynamic Capabilities of ANSYS*, ANSYS 2002 Conf. (2002).

[57] D. V. Anez, C. Hadji, E. Santanach, E. Lorenceau, and C. Picard, *Microfluidic Channels of Adjustable Height Using Deformable Elastomer*, Microfluid. Nanofluidics 1 (2021).

[58] D. H. Kim, J. Song, M. C. Won, H. S. Kim, R. H. Kim, Z. Liu, Y. Y. Huang, K. C. Hwang, Y. W. Zhang, and J. A. Rogers, *Materials and Noncoplanar Mesh Designs for Integrated Circuits with Linear Elastic Responses to Extreme Mechanical Deformations*, Proc. Natl. Acad. Sci. U. S. A. **105**, 18675 (2008).

[59] K. Amit, A. Assam, and A. Raj, *Pressure-Flow Characteristics of a Microchannel Combining Super-Hydrophobicity and Wall Compliance*, Microfluid. Nanofluidics **27**, (2023).

[60] E. Evans and A. Yeung, *Apparent Viscosity and Cortical Tension of Blood Granulocytes Determined by Micropipet Aspiration*, Biophys. J. **56**, 151 (1989).

[61] T. Khamdaeng, J. Luo, J. Vappou, P. Terdtoon, and E. E. Konofagou, *Arterial Stiffness Identification of the Human Carotid Artery Using the Stress–Strain Relationship in Vivo*, Ultrasonics **52**, 402 (2012).

[62] I. C. Christov, V. Cognet, T. C. Shidhore, and H. A. Stone, *Flow Rate-Pressure Drop Relation for Deformable Shallow Microfluidic Channels*, J. Fluid Mech. **841**, 267 (2018).

[63] Z. Wang, A. A. Volinsky, and N. D. Gallant, *Crosslinking Effect on Polydimethylsiloxane Elastic Modulus Measured by Custom-Built Compression Instrument*, J. Appl. Polym. Sci. **131**, 1 (2014).

[64] Z. Zhang, J. Xu, and X. Chen, *Predictive Model for the Cell Passing Pressure in Deformation-Based CTC Chips*, in *ASME International Mechanical Engineering Congress and Exposition*, Vol. 46590 (2014), p. V010T13A043.

[65] H. Hong, E. Yeom, H. S. Ji, H. D. Kim, and K. C. Kim, *Characteristics of Pulsatile Flows in Curved Stenosed Channels*, PLoS One **12**, (2017).

[66] S. Dmitrieff, A. Alsina, A. Mathur, and F. J. Nédélec, *Balance of Microtubule Stiffness and Cortical Tension Determines the Size of Blood Cells with Marginal Band across Species*, Proc. Natl. Acad. Sci. U. S. A. **114**, 4418 (2017).

[67] G. H. McKinley and M. Renardy, *Wolfgang von Ohnesorge*, Phys. Fluids **23**, 127101 (2011).

[68] H. Aryafar and H. P. Kavehpour, *Drop Coalescence through Planar Surfaces*, Phys. Fluids **18**, (2006).

[69] C. Zhu, M. Ertl, and B. Weigand, *Numerical Investigation on the Primary Breakup of an Inelastic Non-Newtonian Liquid Jet with Inflow Turbulence*, Phys. Fluids **25**, 83102 (2013).

[70] I. C. Christov, *Soft Hydraulics: From Newtonian to Complex Fluid Flows through Compliant Conduits*, J. Phys. Condens. Matter **34**, 063001 (2022).

[71] S. Kume, S. Hama, K. Yamane, S. Wada, T. Nishida, and K. Kurisu, *Vulnerable Carotid Arterial Plaque Causing Repeated Ischemic Stroke Can Be Detected with B-Mode Ultrasonography as a Mobile Component: Jellyfish Sign*, Neurosurg. Rev. **33**, 419 (2010).